Long-wavelength stagnant lid convection with hemispheric variation in lithospheric thickness: Link between Martian crustal dichotomy and Tharsis?

Ondřej Šrámek[1] and Shijie Zhong[1]

[1]   A dynamic link between the early evolution of Tharsis and the crustal dichotomy on Mars was recently proposed by Zhong (2009). We address in detail the fundamental aspects of the proposed model using 3-D spherical shell modeling of convection. We investigate the conditions under which a spherical harmonic degree 1 flow is produced in the mantle of Mars in layered viscosity models with different depths of viscosity layering and different viscosity ratios between the bottom and top layers. We find that a thinner weak layer requires a larger viscosity decrease in order to produce degree-1 planform, in qualitative accordance with existing analytical studies. A lithospheric keel of hemispheric extent, which may represent melt residue after dichotomy formation process, is then introduced in the models. As a consequence, thermal upwellings are first formed and oriented below the center of the melt residue cap. For keels of maximum thickness ≳100 km, a rotation of the entire single-plate lithosphere relative to the underlying mantle follows until the plume is stabilized near the edge of the keel, which can be identified as the dichotomy boundary. This model may explain the early migration of the Tharsis volcanic center from southern latitudes to the vicinity of the dichotomy boundary. For keels ≳200 km thick, the modeled time scales agree with observationally inferred migration rate. If the Tharsis migration is caused by the rotation of the lithosphere, the requirement on the amount and location of upper mantle melting would argue for an endogenic origin of the dichotomy.

1.   Introduction

[2]   Taking even a brief look at the topographic map of Mars, one notices two major, global-scale physiographic features. One is the difference in mean elevation between the northern and the southern hemispheres, referred to as the hemispheric dichotomy. The other, the Tharsis Rise, is a large elevated region near the equator in the western hemisphere that comprises several large volcanoes. The origin of the dichotomy as well as the nature of the Tharsis volcanic province are still being debated.

[3]   Using Mariner 9 and earlier data, *Hartmann* [1973] discussed the bimodal character of the hypsometric curve (i.e., histogram of surface elevation) on Mars. He suggested two distinct petrological blocks for the lowlands and highlands crust, akin to the Earth's continental rafts floating in a denser oceanic material. *Schubert and Lingenfelter* [1973] proposed that a difference in crustal thickness is the most likely candidate to explain the center of mass–center of

figure offset. This picture was refined as the data obtained during the 1996–2006 Mars Global Surveyor (MGS) mission became available. Based on analysis of the Mars Orbiter Laser Altimeter (MOLA) data [*Zuber et al.*, 1992; *Smith et al.*, 1998, 1999a] and the MGS gravity field measurements [*Tyler et al.*, 1992; *Smith et al.*, 1999b], *Zuber et al.* [2000] showed that the north-south hemispheric asymmetry in topography is well explained as a manifestation of isostatically compensated crust with lateral thickness variations. The two maxima on the crustal thickness distribution curve are separated by ~26 km, which results in ~5.5 km difference in elevation [*Neumann et al.*, 2004; *Watters et al.*, 2007], as measured by MOLA [*Smith et al.*, 2001]. The abrupt elevation difference across the dichotomy boundary is between 2 and 4 km [*Frey et al.*, 1998], and is superimposed on a more gentle north-to-south pole slope. An expression of the hemispheric dichotomy is found also in the magnetic field [*Purucker et al.*, 2000], surface age pattern and the surface geology in general [*Tanaka*, 1986; *Tanaka et al.*, 1992].

[4]   *Watters et al.* [2007] provided a detailed summary on the crustal ages and the dichotomy formation time. The cratered southern highlands of Noachian age are the oldest exposed rocks. The surface age of the northern smooth

---

[1]Department of Physics, University of Colorado at Boulder, Boulder, Colorado, USA.

plains is mostly Amazonian (<3 Ga, using the dating of Martian epochs from *Solomon et al.* [2005] and *Nimmo and Tanaka* [2005]), but these surficial sediments were deposited over the older ridged plains of early Hesperian (Hesperian epoch spans 3.7–3 Ga) volcanic material [*Withers and Neumann*, 2001; *Head et al.*, 2002]. The MOLA topography data revealed a large circular depression in the Utopia Planitia correlated with a large positive free air gravity anomaly, as well as a number of quasi-circular depressions (QCD) in the northern hemisphere, interpreted as buried impact craters. This suggested that the original lowlands crust is old. The MARSIS (Mars Advanced Radar for Subsurface and Ionospheric Sounding) instrument on the Mars Express spacecraft has provided data on the relief of the buried basins [*Picardi et al.*, 2005]. Crater ages determined from both MGS and MARSIS data give an early Noachian age (4.08–3.93 Ga) for the ancient northern lowlands crust [*Watters et al.*, 2007]. The crater count density of the southern highlands suggests an older age for the highland crust [*Frey*, 2006a, 2006b], even though the age difference may be as small as 100 Myr [*Frey*, 2006b]. The dichotomy formed early in Martian geologic history before the Utopia basin formation in early Noachian [*Watters et al.*, 2007]. *Nimmo and Tanaka* [2005] date the dichotomy formation at 4.12 Ga or earlier, and *Solomon et al.* [2005] suggest an even older age of ~4.5 Ga.

[5] As much as there is a general agreement on the dichotomy formation time, and on the interpretation of the present-day north-south elevation difference as a result of isostatically compensated crust of bimodal thickness distribution, disagreement exists to explain how the dichotomy formed. The models of exogenic origin try to explain the dichotomy as a result of a megaimpact or several large impacts. The hypothesis that the Borealis basin was shaped by a single giant impact was put forward by *Wilhelms and Squyres* [1984]. *Frey and Schultz* [1988] pointed out a problem with a single impact origin; a significantly higher number of large impact basins than is observed would be expected if the Borealis basin represents the largest impact basin within a −2 power law crater size distribution. Instead, their alternative hypothesis involves a cumulative effect of many large impacts. However, then a problem arises as to how to explain the focusing of impacts in one hemisphere.

[6] The single giant impact idea was revived in a recent series of papers [*Andrews-Hanna et al.*, 2008; *Nimmo et al.*, 2008; *Marinova et al.*, 2008] that offer some quantitative tests of the impact hypothesis. *Andrews-Hanna et al.* [2008] try to trace the original location of the dichotomy boundary in the western hemisphere, subsequently overlain by Tharsis, by separating the Tharsis load and the pre-Tharsis component of the present-day topography and gravity fields, in order to reconstruct the original shape of the dichotomy boundary. *Marinova et al.* [2008] present a series of 3-D smoothed particle hydrodynamics (SPH) calculations, and find a set of parameters (namely, impact energy, impact velocity and impact angle) that reasonably explain the observed characteristics of the lowlands basin. *Nimmo et al.* [2008] argue on the basis of 2-D axisymmetric modeling that the impact can explain the decline in magnetic field strength at the impact antipode, as well the petrological signature of the lowlands crust.

[7] However, this new giant impact hypothesis is not without problems. First, the models by *Marinova et al.* [2008] and *Nimmo et al.* [2008] all predicted significant (>100%) variations in ejecta thickness, i.e., >100% crustal thickness variations in the southern hemisphere. To reconcile with observed relatively uniform crustal thickness in the southern hemisphere, these models would require either crustal flow or erosion processes to redistribute the ejecta. However, it is unclear how such processes would lead to uniform crustal thickness in the southern hemisphere, while maintaining the impact basin boundaries intact, given that the topographic gradient is largest at the basin boundaries. Second, recovering pre-Tharsis dichotomy boundary via removing Tharsis loads using present-day gravity and topography data is a challenge. The outcome depends significantly on elastic plate thickness [*Andrews-Hanna et al.*, 2008], and also possibly temporal and lateral variations in elastic thickness. The latter two effects have not been explored. Third, there is a mismatch between the giant impact site locations inferred by *Andrews-Hanna et al.* [2008] (208°E, 67°N) based on topography-gravity analysis, and by *Nimmo et al.* [2008] (170°E, 50°N) that would be consistent with reduced magnetic field. It should be pointed out that *Reese et al.* [2010] proposed an alternative giant impact model to place the impact on the southern hemisphere to explain the crustal dichotomy.

[8] The models of endogenic origin aim to explain the dichotomy as a result of processes related to internal dynamic processes, such as convection in Martian mantle or the core formation early in Martian history. *Mutch and Saunders* [1976] suggested that the difference in crustal thickness is an ancient feature that existed since the completion of the differentiation process. Other models invoke crustal thinning above a single convective upwelling [*Lingenfelter and Schubert*, 1973; *Wise et al.*, 1979]. However, the timing in the crustal thinning model of *McGill and Dimitriou* [1990], which puts the dichotomy formation near Noachian/Hesperian boundary, does not satisfy current time constraints on dichotomy formation.

[9] More recent efforts focused on constraining the conditions necessary to produce a spherical harmonic degree 1 convection. Using Rayleigh-Taylor instability analysis and modeling in axisymmetric spherical geometry, *Zhong and Zuber* [2001] showed that degree-1 flow arises if Martian mantle has an asthenosphere ~100 times weaker than the underlying mantle. *Roberts and Zhong* [2006] extended the modeling into 3-D with temperature- and depth-dependent viscosity, and found that a realistic hundredfold viscosity increase across the mantle including a factor of 25 jump in the midmantle can generate degree-1 flow within 100 Myr. Endothermic phase change in the deep mantle also promotes the lowest degree flow [*Harder and Christensen*, 1996; *Breuer et al.*, 1996], but the much longer time necessary to form a single upwelling is inconsistent with the early formation time for the dichotomy [*Roberts and Zhong*, 2006].

[10] *Sleep* [1994] proposed that the dichotomy is a result of plate tectonic activity, where the original thick crust of northern hemisphere was subducted and a new, thinner crust was produced by spreading from a divergent tectonic boundary. Plate tectonics would stop as a result of cessation of melting at spreading center due to mantle cooling, or alternatively as a result of the resistance of strongly buoyant

young oceanic plate to subduction when the spreading center gets too close to the subduction zone. In a conceptually different plate tectonics model by *Lenardic et al.* [2004] the assumed early plate tectonics episode would be terminated when convective stresses decreased below the yield stress due to mantle warming by highland crust insulation.

[11] *Elkins-Tanton et al.* [2003] showed that solidification of an early magma ocean may result in an unstable density stratification. *Elkins-Tanton et al.* [2005] speculated that a large-scale overturn of the unstable cumulates may result in the formation of the dichotomy. However, no quantitative dynamic model of this process has been presented yet. *Ke and Solomatov* [2006] proposed that a single plume, possibly involved in the dichotomy formation, could have formed in Martian mantle due to a large viscosity contrast between an internally convecting bottom thermal boundary layer and the overlying mantle. Their Rayleigh-Taylor analysis and modeling are similar to an earlier study by *Zhong and Zuber* [2001]. The formation mechanism for the hemispheric dichotomy is still being debated and remains an open question.

[12] The Tharsis region in the western hemisphere is the location of most volcanism on Mars in the last 4 Gyr [e.g., *Banerdt et al.*, 1992; *Tanaka et al.*, 1992]. The buildup of Tharsis postdates the formation of the dichotomy; the bulk volume of volcanic material was deposited over 100–500 Myr, starting a few 100 Myr after the dichotomy formation [e.g., *Phillips et al.*, 2001; *Solomon et al.*, 2005; *Nimmo and Tanaka*, 2005]. Analysis of orientation of tectonic features in the western hemisphere of Mars lead to identification of a timed sequence of tectonic centers; it suggests that an early uplift and volcanism occurred in the highlands of Thaumasia Fossae about 40° south of the present equator, and subsequently migrated northward over a time span of a few hundred Myr to a location near the equator (that is, near the dichotomy boundary) [*Frey*, 1979; *Mège and Masson*, 1996; *Anderson et al.*, 2001]. Migration of volcanic center in Tharsis was also suggested by *Johnson and Phillips* [2005], who compared the spatial pattern of magnetic anomalies to geologic units.

[13] *Hartmann* [1973] noted that Tharsis bears evidence of mantle-induced uplift, and the plume origin hypothesis remains the most likely explanation for Tharsis [*Solomon et al.*, 2005]. Basically, the same, degree-1 convection pattern that was discussed in relation to the dichotomy, is required to explain the localized volcanism of Tharsis. Models that employ endogenic phase transitions to generate degree-1 convection [*Harder and Christensen*, 1996; *Breuer et al.*, 1996] suffer the same inconsistency for Tharsis as for the dichotomy: too long a formation time, when compared to inferred ages, and viscosity layering thus seems to be the best candidate to explain a long-lived upwelling below Tharsis [*Roberts and Zhong*, 2006]. An alternative mechanism for Tharsis formation near the dichotomy boundary that invokes "edge-driven convection" [*King and Anderson*, 1998] was proposed [*King and Redmond*, 2005]. It requires a sharp change in lithospheric thickness along the dichotomy boundary which drives small-scale convection that generates melt [*King*, 2010]. The challenge for this mechanism is to satisfy the constraint of the total volume of igneous material ~3×10^8 km^3 [*Phillips et al.*, 2001], as well as to explain the

localized but long-lived volcanism in the Tharsis volcanic province.

[14] Both the hemispheric dichotomy and Tharsis are primarily spherical harmonic degree 1 structures. The early migration of the Tharsis volcanic center and the relative locations of Tharsis and the dichotomy boundary motivated *Zhong* [2009] to suggest a dynamical link between these two structures. In his model, a thicker lithosphere in the current southern hemisphere is assumed to have resulted from some process accompanied by partial melting, which led to the formation of the thick crust. This could be, for example, partial melting above a single dominant upwelling in the mantle [*Roberts and Zhong*, 2006] or a large-scale overturn of post magma ocean cumulates accompanied by decompression melting [*Elkins-Tanton et al.*, 2005]. The thick lithospheric keel in one hemisphere thus represents a residue after melting and is expected to have an increased viscosity due to devolatilization [e.g., *Pollack*, 1986]. With a realistic temperature and depth dependence of viscosity and a step viscosity increase in midmantle, which produces convective planform with a single upwelling [*Roberts and Zhong*, 2006], *Zhong* [2009] reports (1) formation of the upwelling, initially centered below the thick lithospheric keel; (2) subsequent differential movement between the entire lithospheric shell and the upwelling, during which the plume moves toward the edge of the lithospheric keel; (3) and final stabilization of the plume near the keel boundary (i.e., the dichotomy boundary). This model therefore dynamically relates the formation of Tharsis to the preexisting crustal dichotomy. It may explain the early migration of Tharsis with respect to the dichotomy, and its subsequent long-term stabilization at the current location near the dichotomy boundary.

[15] The goal of this study is to systematically address the aspects of *Zhong*'s [2009] model. In the first part we investigate the convective planform of models with uniform lithospheric thickness. We focus on the effect of varying the thickness of the weak layer in models with viscosity layering, and identify the conditions under which degree-1 convection forms. This supplements previous work by *Roberts and Zhong* [2006], who kept the weak layer thickness unchanged. Second, we extend the models by including a lithosphere of variable thickness and study the relative rotation of the lithosphere and the deeper mantle. In section 2 we describe the model setup. The results for models with uniform lithospheric thickness and with lateral variation in lithospheric thickness are presented in sections 3 and 4, respectively. Discussion follows in section 5, where we first address the more general aspects inherent in our models, such as the preferred wavelength of convection, modulation of convective planform by partial surface insulation, and the interaction of mantle flow and lithospheric thickness variations, before discussing specific questions related to Martian evolution. In section 6 we summarize the main findings.

2. Model Description

[16] We investigate thermal convection in 3-D spherical shell representing Martian mantle using CitcomS [*Zhong et al.*, 2000, 2008]. The setup is identical to the models of *Roberts and Zhong* [2006]. The incompressible mantle

Table 1. Parameters of Convection Calculations

Parameter	Value	Unit
Planetary radius	3400	km
Core radius	1650	km
Gravitational acceleration	3.73	m s^{-2}
Mantle density	3400	kg m^{-3}
Thermal diffusivity at CMB	2×10^{-6}	m^2 s^{-1}
Thermal diffusivity at surface	1×10^{-6}	m^2 s^{-1}
Thermal expansivity at CMB	2×10^{-5}	K^{-1}
Thermal expansivity at surface	4×10^{-5}	K^{-1}
Specific heat at constant pressure	1200	J K^{-1} kg^{-1}
Surface temperature	220	K
CMB temperature	2200	K
Activation energy	157	kJ mol^{-1}
Activation volume	2.69	cm^3 mol^{-1}
Volumetric heat source	7.4×10^{-8}	W m^{-3}

under the extended Boussinesq approximation [*Christensen and Yuen*, 1985] is heated both from within and from below. The nondimensionalized governing equations are

$$\nabla \cdot \mathbf{v} = 0, \tag{1}$$

$$-\nabla P + \nabla \cdot \left[\eta \left(\nabla \mathbf{v} + \nabla^T \mathbf{v} \right) \right] + Ra\,\alpha(r) T \mathbf{e}_r = 0, \tag{2}$$

$$\frac{\partial T}{\partial t} + \mathbf{v} \cdot \nabla T = \nabla \cdot [\kappa(r)\nabla T] + H_{int} + H_A + H_V, \tag{3}$$

where $\mathbf{v}$ is the velocity vector, P is the pressure, T is the temperature, η is viscosity, and $\mathbf{e}_r$ is a unit vector in the radial direction. The three source terms in equation (3) are rates of radiogenic (H_{int}), adiabatic (H_A) and viscous (H_V) heating. The depth-dependent thermal conductivity $\alpha(r)$ and thermal diffusivity $\kappa(r)$ are assumed to be linear functions of radius. The Rayleigh number Ra is defined as

$$Ra = \frac{\rho_0 \alpha_0 \Delta T g R_0^3}{\kappa_0 \eta_0}, \tag{4}$$

where ρ_0, α_0, κ_0, and η_0 are the reference values for density, thermal expansivity, thermal diffusivity, and viscosity. The reference values are those at the bottom of the mantle. The other three parameters in equation (4) are the gravitational acceleration g, the temperature difference across the mantle ΔT, and the radius of the planet R_0.

[17] Isothermal, free slip boundary conditions are imposed on top and bottom boundaries, unless noted otherwise. Parameters of the calculations are listed in Table 1. Viscosity is pressure- and temperature-dependent according to [*Roberts and Zhong*, 2006, equation (8)]

$$\eta = \eta' \exp\left[\frac{E + V(1-r)}{T + T_s} - \frac{E + V(1-r_{cmb})}{1 + T_s} \right], \tag{5}$$

where r is the nondimensional radial position and r_{cmb} is the nondimensional bottom boundary radius (i.e., the core-mantle boundary). The nondimensional parameters E, V and T_s are calculated from the dimensional values of the activation energy E^*, activation volume V^* and surface temperature T_{surf}, using

$$E = \frac{E^*}{R\Delta T}, \quad V = \frac{\rho_0 g R_0 V^*}{R\Delta T}, \quad T_s = \frac{T_{surf}}{\Delta T}, \tag{6}$$

where R is the universal gas constant.

[18] A step increase in viscosity at a given depth is introduced through the radial viscosity prefactor $\eta'(r)$, which is a piecewise constant function of radius. We vary the depth of viscosity layering d_l as well as the lower to upper mantle viscosity ratio $\mathcal{R}_\eta = \eta_{LM}/\eta_{UM}$. *Roberts and Zhong* [2006] placed the depth of viscosity layering in all their models at 1020 km. For Mars this depth corresponds to the pressure of the phase transition occurring near the top of the transition zone (around 410 km depth) in Earth. Here, we vary the thickness of the weak layer.

[19] In models without an imposed lithospheric keel (section 3) we let the lithosphere of nearly uniform thickness arise naturally from the temperature dependence of viscosity. In models with imposed lateral variations in lithospheric thickness (section 4), the treatment of the lithosphere exploits the thermochemical capability of CitcomS [*McNamara and Zhong*, 2004]. We initially define the lithosphere as a chemical layer of concentration equal to 0 while the mantle material is assigned concentration equal to 1. The concentration is evolved using the ratio tracer method [*Tackley and King*, 2003; *McNamara and Zhong*, 2004]. We use a global lithospheric layer of uniform thickness 40 km, onto which a lithospheric keel is added. We use a keel of lateral extent of 90 angular degrees (i.e., a hemispheric extent). We vary the maximum thickness and the exact shape of the keel, but in most of our models the keel is thickest at its center and its thickness decreases with increasing angular distance from the center. The lithosphere is set up to represent the residue left after partial melting that had formed the crust. The lithospheric keel thus corresponds to larger amount of melting and thicker crust in one hemisphere and approximates the dynamic effect of the hemispheric dichotomy. It is reasonable to assume that the melting process depleted the residual lithospheric material in incompatible volatile species such as hydrogen and CO_2, thus causing stiffening [*Pollack*, 1986; *Hirth and Kohlstedt*, 1996]. Therefore in the combined lithospheric shell (i.e., the uniform layer plus the keel), the viscosity is increased, by a factor of 200, with respect to the lower mantle viscosity. Figure 1 shows the lithosphere geometry for one particular keel shape.

[20] The models with uniform lithosphere were started from a compatible radial temperature profile (*Roberts and Zhong* [2006], *Zhong* [2009], using results from previous calculations in our group) and a superimposed random perturbation. Each case was run until a stable convective planform was attained. The models with lateral variation in lithospheric thickness were started from a given time step of the models with uniform lithosphere with corresponding viscosity profile and other model parameters. The 3-D spherical shell was divided into twelve caps horizontally and
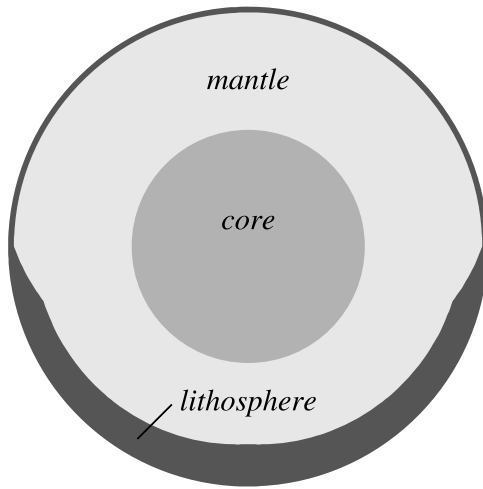
Figure 1. Configuration with keel B (Table 4). Thickness of the lithosphere is exaggerated by a factor of 2.

two layers in vertical for parallel computing. The finite element grid in each of the 24 segments contains 48 elements in each horizontal direction and 24 elements in the vertical direction, leading to a total of about 1.3×10^6 elements. The grid was refined in the vertical direction in the thermal boundary layers. Each calculations used 24 computing nodes on a cluster with AMD Opteron processors. The modeling results are presented in sections 3 and 4.

3. Models With Uniform Lithospheric Thickness

[21] The suite of models in this section is designed to investigate how the convective planform of layered viscosity models changes with the depth of layering and the magnitude of viscosity contrast, and in particular what are the conditions for spherical harmonic degree 1 convection, which is needed in the rotation of the lithosphere model [*Zhong*, 2009]. Our knowledge of the viscosity structure of Martian interior is quite limited. Viscosity layering of the Martian mantle has been suggested, but the layering depth as well as the viscosity contrast are not well constrained. It is therefore useful to perform a study of the preferred convection wavelength dependence on these two parameters. Of

course, this issue is also of general fluid dynamics interest. The cases presented here extend the previous analysis of *Roberts and Zhong* [2006], where the depth of viscosity layering was kept constant. The input parameters and some output values of the computed cases are shown in Table 2.

[22] We start with a case TC1, which is identical to 'Model 1' of *Zhong* [2009] and 'Case V3' of *Roberts and Zhong* [2006]. It includes a 25-fold viscosity increase at 1020 km depth. Run 'a' of case TC1 (hereafter denoted TC1_a) started from initial radial temperature profile with somewhat higher temperatures compared to the final state of this case, and a spherical harmonic degree 11 horizontal perturbation. The average nondimensional temperature $\langle T \rangle$ decreased from 0.739 to 0.712 at the end of the calculation. Degree 1 dominates the spherical harmonic spectrum, calculated 100 km above run core-mantle boundary, starting at time 630 Myr and remains so for the rest of calculation (Figure 2a). Run 'b' of case TC1 (denoted TC1_b) started from an initial radial temperature profile close to the final profile for this case, and a random perturbation. The average temperature $\langle T \rangle$ slightly decreases from 0.717 to 0.715. Degree 1 becomes the strongest at 470 Myr (Figure 2b). The final states from runs TC1_a and TC1_b are identical, thus confirming that the initial condition has no effect on the final convective planform. Our results are also in agreement with 'Case V3' of *Roberts and Zhong* [2006]. Horizontally averaged temperature $\langle T \rangle_h$ away from the boundary layers varies between ~0.7 in the topmost mantle and ~0.8 in the deep mantle (Figure 3a). The temperature drop across the upper thermal boundary layer is larger than for the bottom boundary layer due to the large contribution of internal heating to the total heating (~82%). The total viscosity increase across the mantle, including the step increase at 1020 km depth, is by a factor of ~130 (Figure 3b). The final thermal structure, shown in Figures 4a–4b, is a single localized upwelling. The flow field evolves to the final state through a stage with a circumferential sheet-like upwelling (Figure 4c). The thermal anomalies are strongest in the boundary layers, within 100–150 km of the top and bottom boundaries. Spherical harmonic degree 1 is the strongest at all depths in the final state; the near-surface temperature field has a strong degree 2 component.

[23] Case TC2 is identical to TC1 except for a shallower viscosity layering, which occurs at depth 770 km instead of

Table 2. Input Parameters and Some Output Values for Cases With Uniform Lithospheric Thickness[a]

Case	d_l (km)	$\mathcal{R}_\eta$	Ra	Steps	t_{end} (Gyr)	$\langle T \rangle$	$\Delta\eta$	Internal Heating (%)	l
TC1_a	1020	25	1.25×10^8	100,000	1.23	0.712	130	82	1
TC1_b	1020	25	1.25×10^8	69,700	0.89	0.715	130	82	1
TC2	770	25	1.25×10^8	45,000	0.58	0.711	140	81	2
TC21_a	770	50	1.25×10^8	48,000	0.46	0.692	290	81	1
TC21_b	770	50	1.25×10^8	134,000	1.94	0.686	290	80	1
TC3	520	25	1.25×10^8	127,700	1.44	0.709	140	78	4,8
TC31	520	50	1.25×10^8	100,000	1.16	0.679	290	76	2–4
TC32	520	100	1.25×10^8	126,300	1.07	0.651	590	75	2
TC33	520	200	1.25×10^8	187,700	1.22	0.617	1200	77	1

[a]Here, d_l, depth of layering; $\mathcal{R}_\eta$, viscosity ratio; Ra, input Rayleigh number; t_{end}, time at the end of calculation; $\langle T \rangle$, average temperature; $\Delta\eta$, viscosity increase across the mantle; l, dominant spherical harmonic degree.
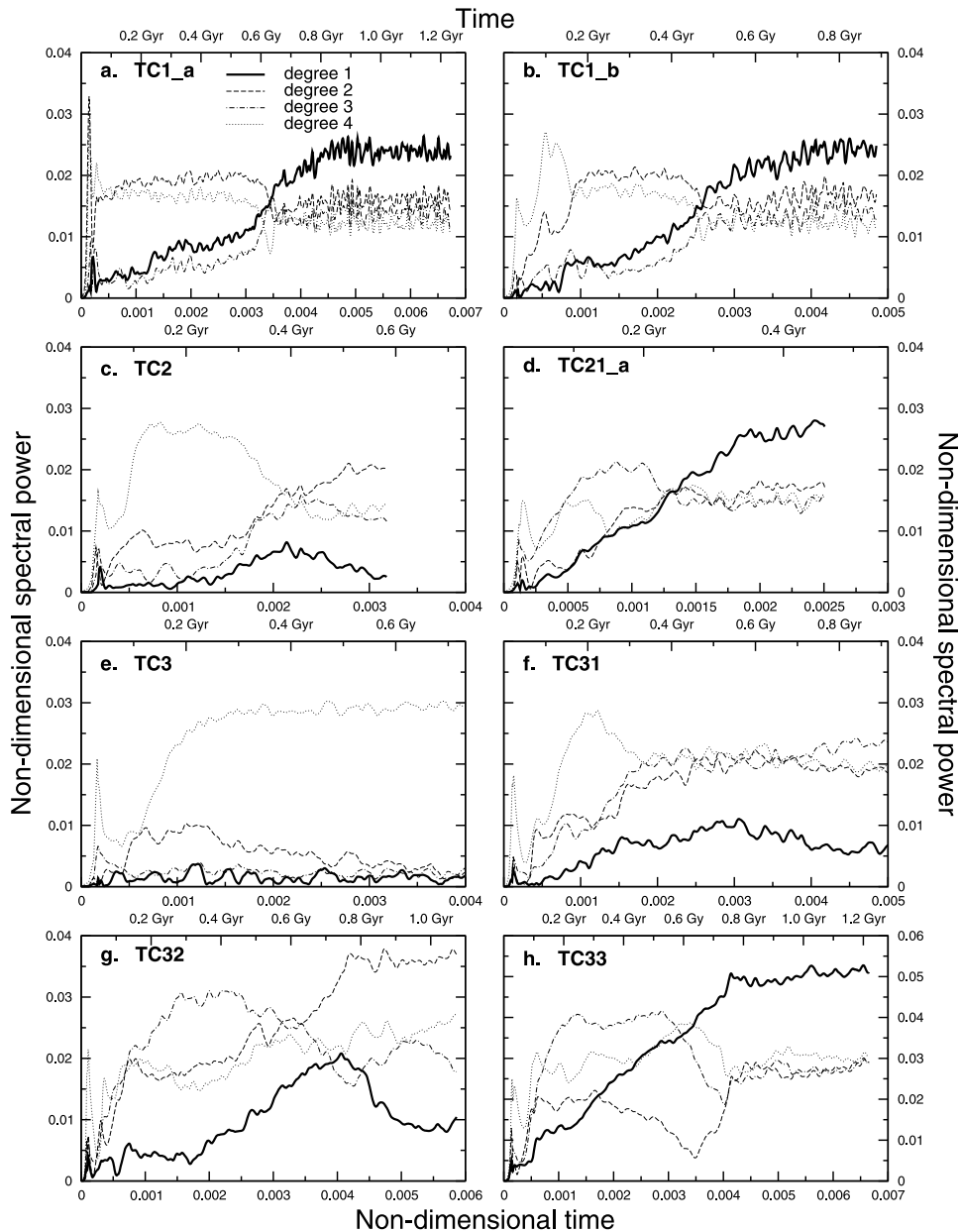
Figure 2. Time dependence of spherical harmonic spectra, calculated 100 km above the bottom boundary, for cases with uniform lithospheric thickness. (a) TC1_a, (b) TC1_b, (c) TC2, (d) TC21_a, (e) TC3, (f) TC31, (g) TC32, and (h) TC33.

1020 km. It is started from the same initial condition as case TC1_b. With a viscosity decrease in the upper layer by a factor 25, the thermal structure develops into a state with an upwelling plume, and an elongated sheet-like upwelling in the opposite hemisphere (Figure 4d). Accordingly, degree 2 dominates the spherical harmonic spectrum at all depths (Figure 2c). The final average temperature $\langle T \rangle$ is 0.711 and the depth dependence of horizontally averaged temperature $\langle T \rangle_h$ is identical to case TC1 (Figure 3a), leading to a similar viscosity increase across the mantle by a factor of 140.

[24] We examined whether a larger viscosity contrast will favor convection with a dominant degree 1. Case TC21 differs from TC2 by a larger viscosity decrease in the upper layer by a factor of 50 instead of 25. Run 'a' (TC21_a)

started from a radial temperature profile hotter than the final state for this case, while run 'b' (TC21_b) from an overall colder initial temperature. In both cases a single elongated, ridge-like upwelling structure develops (Figure 4e). For this final state spherical harmonic degree1 is dominant at all depths. It took ~250 Myr for the degree-1 planform to develop in run TC21_a (Figure 2d), while a much longer time, ~1.4 Ga, in run TC21_b due to the larger mantle viscosity. This confirms again that the final state is independent from the initial condition, but we observe a large difference in the time it takes to attain the final degree-1 planform. Since planets are formed hot at the end of the accretion and are expected to continuously cool down during their early evolution, it is the shorter time scale of TC21_a
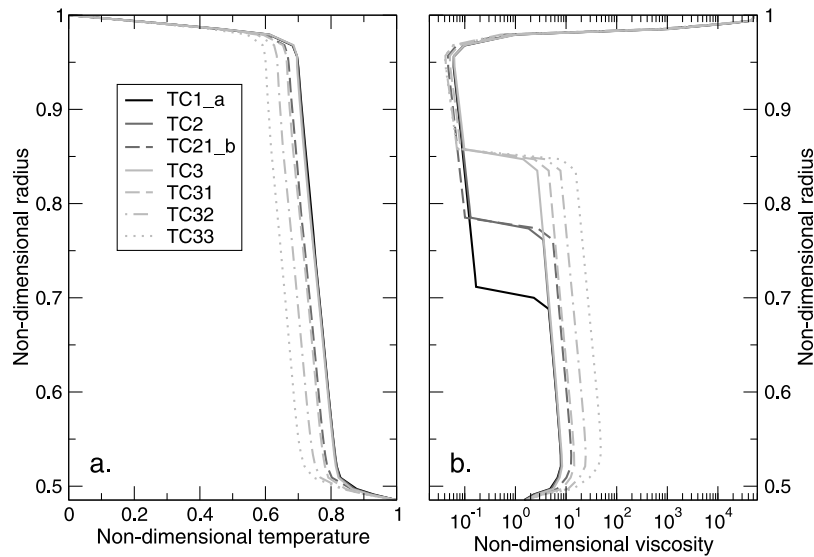
Figure 3. Horizontally averaged (a) temperature and (b) viscosity for cases with uniform lithospheric thickness.

with a hotter initial temperature that is geophysically relevant. Temperature in the convective core away from thermal boundary layers is smaller than in cases TC2 and TC1 (which have smaller imposed viscosity contrast) by ~0.03 (60 K) (Figure 3a). The lower mantle viscosity is increased by a factor of ~1.4 relative to case TC2, while the upper mantle viscosity is decreased by a similar factor; this yields an overall viscosity increase by a factor of 290 across the mantle (Figure 3b).

[25] We further decrease the thickness of the upper weak layer by placing the viscosity step at depth 520 km. The cases in series TC3, TC31, TC32, and TC33 have a gradually increasing viscosity ratio of 25, 50, 100, and 200, respectively. The final horizontally averaged temperature $\langle T \rangle_h$ of case TC3 with a 25-fold step increase in viscosity matches very closely the profiles for cases TC1 and TC2 with identical magnitude of viscosity change (Figure 3a). The total viscosity increase across the mantle is by a factor of 140. For case TC3, most spectral power is at degrees 4 at all depths (Figure 2e); above the bottom thermal boundary degree 8 is also significant. The thermal structure features 6 evenly spaced upwellings, pointing approximately toward the vortices of a regular octahedron (Figure 4f).

[26] Case TC31 has the viscosity contrast at 520 km depth increased to 50. The final average temperature in the mantle is lower than in case TC3 by ~0.03 (60 K), and is similar to case TC21 that has the same imposed viscosity contrast. Viscosity increase with respect to TC3 in lower mantle by a factor ~1.6 is somewhat stronger than viscosity decrease in the upper layer by a factor ~1.3. Overall viscosity increase across the mantle is 290-fold. Most spectral power is at degrees 2–4 (Figure 2f), degree 2 being the strongest in lower mantle and degrees 3 and 4 dominant in middle to upper mantle. The structure contains several plumes and a ridge-like upwelling (Figure 4g).

[27] In case TC32 the viscosity contrast is further increased to 100. The resulting average mantle temperature is lower than in TC3 by ~0.07 (130 K). Lower mantle vis-

cosity is increased by a factor of ~3.1 with respect to TC3, while the upper layer viscosity is lower by a factor ~1.4, yielding an overall viscosity increase by 590 in the mantle. The final thermal structure has a localized plume and an antipodal ridge-like upwelling, and degree 2 is the strongest at all depths (Figures 4h and 2g).

[28] In order to observe convection at dominant spherical harmonic degree 1, the imposed viscosity contrast has to be increased to 200, which was done in case TC33. Final temperature in the mantle is lower by ~0.11 (220 K) compared to case TC3, lower layer viscosity is increased by a factor of ~6, and upper layer viscosity decreased by a factor of ~1.4; across-the-mantle viscosity increase is by a factor of 1200. Degree 1 becomes the strongest at all depths at 630 My (Figure 2h) and the thermal structure is dominated by a single upwelling with 3 ridge-like flanks (Figure 4i).

[29] As the imposed viscosity jump is increased, within each series of cases with constant depth of layering d_l (i.e., series TC2—TC21 and TC3—TC33) the temperature of the mantle decreases. Accordingly, the viscosity in the lower mantle increases. However, the upper layer becomes progressively weaker. This is because the step decrease in viscosity more than compensates for the lower temperature (Figure 3b). The weaker upper layer leads to higher surface heat flux, therefore faster cooling, which explains the lower interior temperature. The regime diagram in Figure 5 summarizes the computed cases as a function of the nondimensional layering depth d_l/R_0 and the viscosity contrast $\mathcal{R}_\eta$.

4. Models With Lateral Variations in Lithospheric Thickness

[30] In this section we include a lithospheric keel that represents the stiff residue left after partial melting which may be responsible for the formation of thickened crust in one hemisphere of Mars (i.e., the hemispheric dichotomy). This keel introduces strong lateral variations in viscosity near the surface. The goal is to investigate the effect of
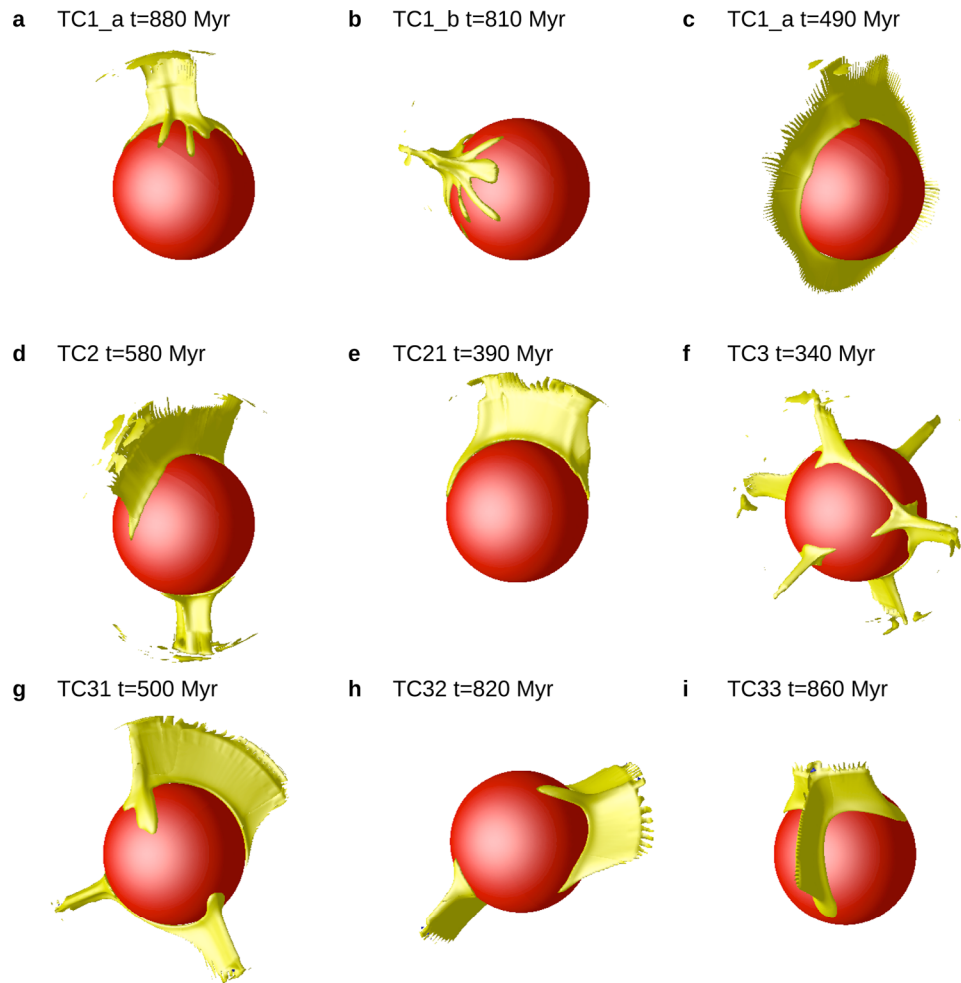
Figure 4. Isosurface of residual temperature at $T = +0.04$ (Figures 4a–4c), $T = +0.03$ (Figures 4d–4g), and $T = +0.06$ (Figures 4h–4i) in yellow; in red is core surface. Temperature in the uppermost 120 km is not plotted. (a) TC1_a at 880 Myr (time step 60,000), (b) TC1_b at 810 Myr (60,000), (c) TC1_a at 490 Myr (30,000), (d) TC2 at 580 Myr (45,000), (e) TC21 at 390 Myr (40,000), (f) TC3 at 340 Myr (25,000), (g) TC31 at 500 Myr (50,000), (h) TC32 at 820 Myr (100,000), and (i) TC33 at 860 Myr (130,000).

various parameters on the rotation of the lithosphere, reported by *Zhong* [2009]. Among the questions we want to address are: What is the effect of imposed degree-1 lithospheric thickness variation on the models presented in section 3? How thick does the lithospheric keel need to be in order to excite lithospheric rotation? Is any particular shape of the keel needed for the rotation? In this section we mainly present the results; most of the discussion is postponed until section 5.

[31] Parameters of all presented cases are listed in Table 3. Case TC1A is set up identically to TC1 of section 3 (i.e., 25-fold viscosity step at 1020 km depth) and includes a lithospheric keel A: its maximum thickness is 260 km at the center and decreases linearly to zero at angular distance 90° (see Table 4 for the geometrical setup of different keels). This case corresponds to 'Model 2' of *Zhong* [2009]. The initial temperature field is an early state of a TC1 calculation from section 3, and has a spherical harmonic degree 2 character (Figure 6a). After nondimensional time $t \sim 3 \times 10^{-4}$ (60 Myr, time step 5500) degree 1 becomes dominant and at $t \sim 5 \times 10^{-4}$ (90 Myr, time step 8000) a localized

thermal upwelling forms, located below near center of the lithospheric keel. This can be seen on the snapshots on the temperature field (Figures 6b–6c) as well as on the time series of the spherical harmonic power (Figure 7a). Shortly after the upwelling forms (within ~50 Myr), a motion of the entire lithospheric shell with respect to the upwelling is initiated. The average rate of separation during the stage of initial fast rotation is ~0.66°/My (Table 3). The separation rate somewhat decreases when the plume-keel angular distance reaches ~70°. In about 200 Myr, the angular separation between the center of the plume and the center of the lithospheric keel increases from near 0 to near 90° (Figure 6d). At this point the differential movement ceases and the plume remains located near the edge of the lithospheric keel (i.e., at angular separation around 90°). This motion and subsequent stabilization are illustrated in Figure 8a. This case shows the same results as 'Model 2' of *Zhong* [2009].

[32] We have investigated whether this motion is observed with a thinner lithospheric keel. Case TC1A1 has a keel of maximum thickness 130 km (keel A1, see Table 4), which is half of the maximum thickness in case TC1A. It is
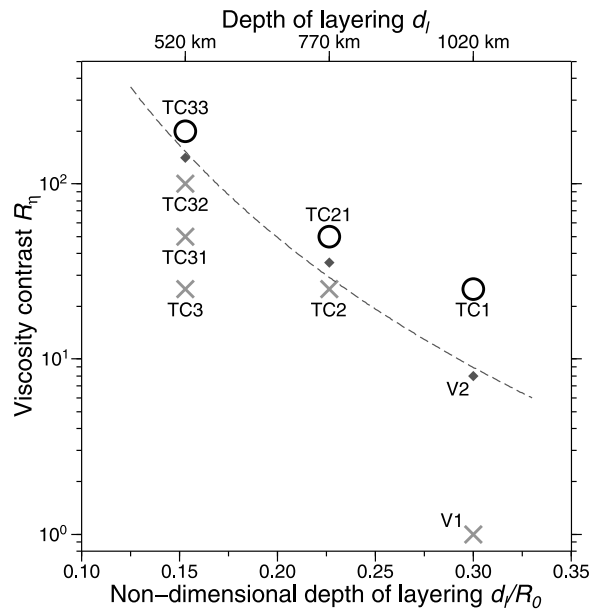
Figure 5. Cases with uniform lithospheric thickness as a function of layering depth d_l and viscosity ratio $\mathcal{R}_\eta$. Cases that develop a degree-1 planform are shown as black circles; cases with shorter wavelength of flow are shown as gray crosses. Data point corresponding to cases V1 and V2 of *Roberts and Zhong* [2006] are labeled accordingly. Midpoints approximating the boundary between $l = 1$ and $l > 1$ regions are plotted as small diamonds and the best fit to equation (9) as dashed curve.

otherwise identical to case TC1A and is started from the same initial state. We observe again a fast concentration of upwellings below the keel center within tens of Myr case, however, the delay between the plume formation and the onset of rotation is larger, about 250 Myr (Figure 6f). Moreover, the average plume-keel separation rate is 3–4 times slower than in case TC1A (~0.21°/Myr compared to ~0.66°/Myr; Figure 8a and Table 3).

[33] We ran a case TC1A2, where the maximum keel thickness is further reduced, equal to 65 km (keel A2). Even then, the flow is quickly organized into a degree 1 structure,

centered below the keel center (Figure 6g). However, the rotation of the lithosphere is now absent and the plume stays centered below the thick lithosphere (Figure 8a). Is there any limit for the lithospheric thickness variation below which the preferential orientation of the upwelling disappears? In case TC1A3, the maximum keel thickness is only 35 km. The upwelling still forms below the keel center (Figure 6h). This is an effect of the keel; a reference case with uniform lithospheric thickness (i.e., case TC1 with no keel) develops a degree-1 structure that is located in the opposite hemisphere relative to cases with a keel.

[34] In order to resolve the lithospheric thickness variations (i.e., the keel shape), a sufficient number of elements in radial direction must be present in between the minimum and the maximum depth of the base of the lithosphere, which requires fine mesh spacing, especially for thin keels, in the bottom part of the lithosphere, and affects the overall discretization as well as the horizontal to vertical size ratio of individual elements. In case TC1A3, we use 3 radial elements than span the keel thickness of 35 km. Without increasing the total number of elements in the radial direction, this is the minimum keel thickness we can use while still keeping acceptable overall mesh spacing.

[35] Next we investigated how sensitive is the model to the specific shape of the lithospheric keel. We ran two cases with a modified keel shape. Case TC1B uses keel B. The maximum keel thickness is 260 km at the center, the thickness decreases linearly to 160km at angular distance from the center 75°, and then to 0 at angular distance 90° (Table 4 and Figure 1). Case TC1C uses keel C of uniform thickness 160 km for angular distance from the keel center <75° and its thickness decreases linearly to 0 from 75° to 90° (Table 4). Case TC1B shows essentially the same behavior as TC1A. The snapshots of the temperature field (Figures 9a–9c) are very similar to TC1A and the plume-keel separation curve closely follows the trend of TC1A (Figure 8a), yielding a somewhat lower but comparable rate of ~0.46°/Myr. The rotation of the lithosphere is also present in case TC1C. Here the separation rate ~0.24°/Myr is about 3 times slower than in case TC1A, and the rotation ceases somewhat earlier, when the separation is around 70° (Figure 8a).

Table 3. Parameters of Cases With Lithospheric Keel or Low-Conductivity Lid[a]

Case	d_l (km)	$\mathcal{R}_\eta$	Keel	Ra	Steps	t_{end} (Gyr)	Separation Rate (°/Myr)
TC1A	1020	25	A	1.25×10^8	54,100	0.46	0.66
TC1A1	1020	25	A1	1.25×10^8	80,000	0.79	0.21
TC1A2	1020	25	A2	1.25×10^8	80,000	0.61	~0
TC1A3	1020	25	A3	1.25×10^8	45,900	0.45	~0
TC1B	1020	25	B	1.25×10^8	52,000	0.45	0.46
TC1C	1020	25	C	1.25×10^8	72,000	0.57	0.24
TC1B0	1020	25	B	1.25×10^8	80,000	0.70	0.35
TC2B	770	25	B	1.25×10^8	63,600	0.62	0.40
TC21B	770	50	B	1.25×10^8	51,500	0.36	0.9
TC31B	520	50	B	1.25×10^8	42,500	0.41	1.1
TC32B	520	100	B	1.25×10^8	48,200	0.30	1.5
TC33B	520	200	B	1.25×10^8	70,800	0.45	1.5
TC1K	1020	25	$\frac{1}{5}k_T$-lid	1.25×10^8	50,000	0.42	~0
TC1K1	1020	25	$\frac{2}{3}k_T$-lid	1.25×10^8	48,400	0.40	~0

[a]See Table 2 for notation; rates of separation between the center of the upwelling and the center of the lithospheric keel are reported in the last column.

Table 4. Geometry of lithospheric keels

Keel	Maximum Keel Thickness	Variation of Keel Thickness With Angular Distance	Maximum Lithospheric Thickness
A	260 km	Linear decrease from 260 km at the center to 0 at angular distance 90°.	300 km
A1	130 km	Linear decrease from 130 km at the center to 0 at angular distance 90°.	170 km
A2	65 km	Linear decrease from 65 km at the center to 0 at angular distance 90°.	105 km
A3	35 km	Linear decrease from 35 km at the center to 0 at angular distance 90°.	75 km
B	260 km	Linearly decreases from 260 km at the center to 160 km at angular distance 75°, then to 0 at 90°.	300 km
C	160 km	Constant thickness 160 km at angular distance <90°, zero elsewhere.	200 km

[36] As was already discussed by *Zhong* [2009], the rotation of the lithosphere with respect to the upwelling is a robust behavior that occurs even if the motion of the lithosphere itself is prevented. This is illustrated in case TC1B0, which differs from case TC1B by imposing a zero horizontal velocity (i.e., no slip) instead of free slip as the upper boundary condition. Here the lithospheric shell is fixed in space, and it is the upwelling structure that moves consistently away from the keel center at a rate comparable to the separation rate in case TC1B. Then the plume stabilizes at angular distance around 70° (Figure 8a).

[37] In the following we revisit cases TC2, TC21, TC31, TC32 and TC33 from section 3, but include the lithospheric keel B. Case TC2B with 25-fold viscosity reduction above
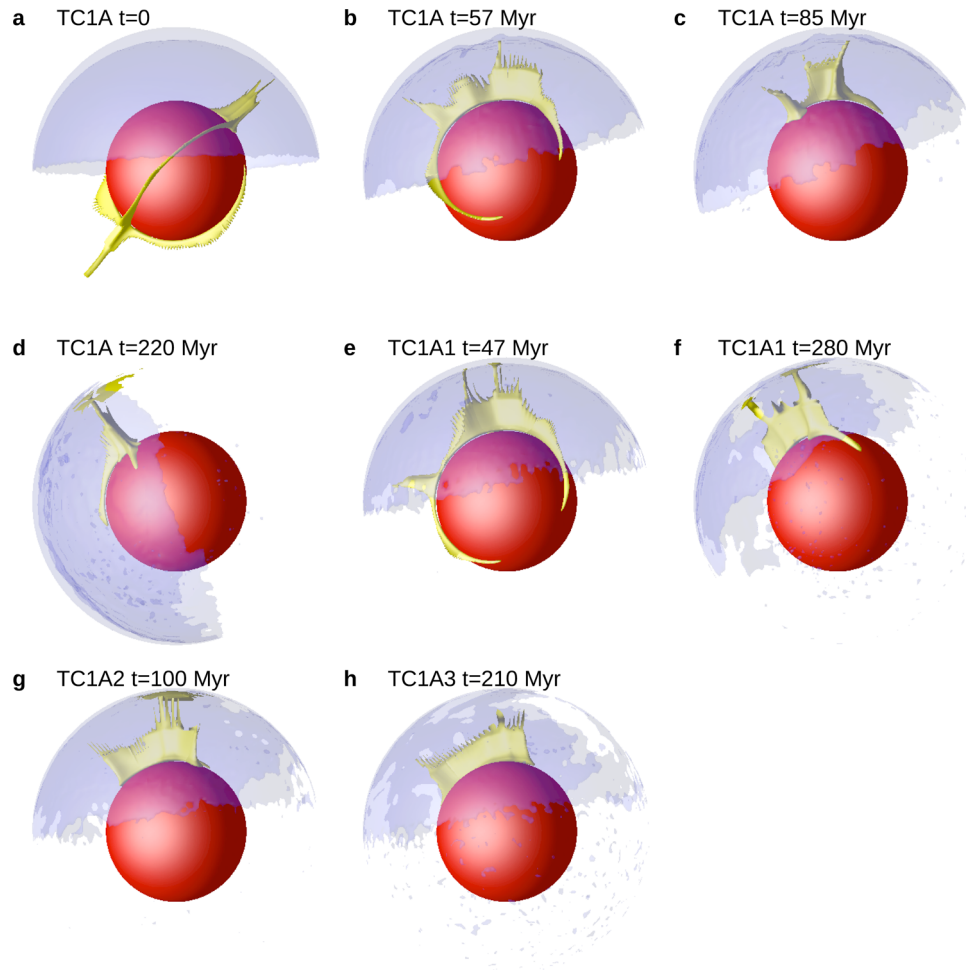

Figure 6. Isosurface of residual temperature at $T = +0.07$ in yellow and contour of the lithospheric keel, corresponding to residual composition isosurface at $C = -0.07$, in opaque blue. Temperature in the uppermost 120 km is not plotted. (a) TC1A initial state, (b) TC1A at 57 Myr (time step 5500), (c) TC1A at 85 Myr (8000), (d) TC1A at 220 Myr (25,000), (e) TC1A1 at 47 Myr (5000), (f) TC1A1 at 280 Myr (30,000), (g) TC1A2 at 100 Myr (10,000), and (h) TC1A3 at 210 Myr (20,000).
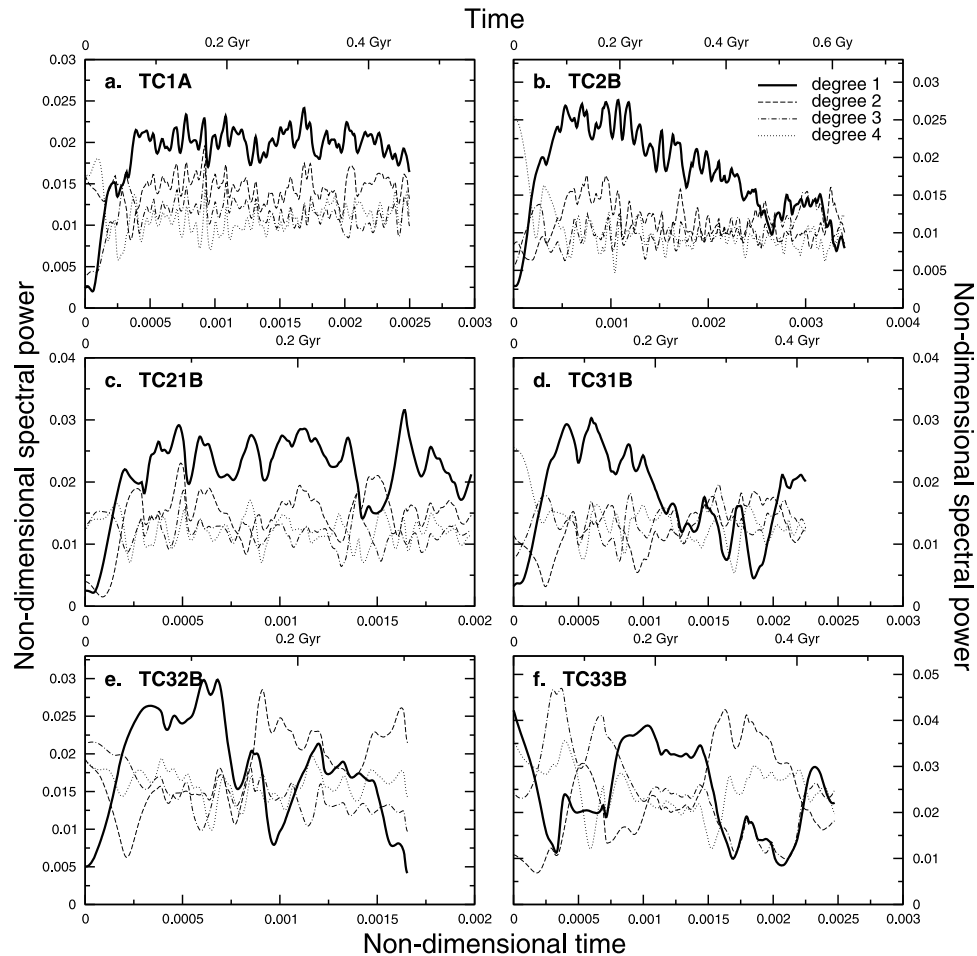
Figure 7. Time dependence of spherical harmonic spectra, calculated 100 km above the bottom boundary, for cases with lithospheric keel. (a) TC1A, (b) TC2B, (c) TC21B, (d) TC31B, (e) TC32B, and (f) TC33B.

770 km depth was started from time step 20,000 of case TC2, with dominant degree 4 (Figure 10a). Imposition of the hemispheric keel resulted in migration of the individual upwellings so that after ~60 Myr all were present below the thickened lithosphere (Figure 10b). Later the individual plumes merged into a single upwelling structure centered within 25° of the keel center; note that without the lithospheric keel, the thermal field assumes a degree 2 character with a ridge and an antipodal plume (Figure 4d for case TC2). Subsequent migration of the lithosphere at an average rate ~0.40°/Myr was observed (Figures 10c and 8b). Later, after ~300 Myr, the upwelling structure develops an elongated, ridge-like shape, from which individual plumes rise (Figure 10d). This ridge is oriented perpendicularly to the keel boundary and the location of the geometric center of the upwelling oscillates between 90° and 130° (Figure 8b). The power at degree 1 decreases with time and at $t \sim 450$ becomes comparable to the other degrees (Figure 7b). Even though in the later stages ($\gtrsim 270$ Myr) the keel-upwelling separation remains approximately constant (Figure 8b), we observe a continuation of the lithospheric rotation where the upwelling rotates together with the lithosphere (about 180° rotation between $t = 270$ Myr and $t = 410$ Myr, seen in Figures 10c–10d). We address this issue in discussion.

[38] Case TC21B was started from step 7000 of case TC21, with viscosity increase by a factor of 50 at a depth of 720 km (Table 3). We observe focusing of upwelling below the keel center from the initial short-wavelength structure within ~30 Myr (Figures 7c and 10e). The lithosphere then rotates with respect to the upwelling at an average rate ~0.9°/Myr, i.e., roughly twice as fast as separation in case TC2B, and rotates to 90° away from the upwelling at $t \sim$ 120 Myr (Figures 10f and 8b). Near the edge of the keel the upwelling is again stretched into an elongated ridge perpendicular to the keel boundary (Figure 10g). Compared to case TC2B, however, the ridge is shorter and the upwelling more compact. This is probably related to the fact that, unlike in TC2B, case TC21B with weaker upper mantle intrinsically develops single upwelling even without a keel (i.e., Figure 4e for case TC21).

[39] Case TC31B with fiftyfold viscosity reduction above 520 km depth was started from time step 15,000 of case TC31. Within ~50 Myr the initially globally distributed upwellings cluster below the thick lithosphere (Figure 10h). The spherical harmonic spectrum of temperature field is dominated by degree 1 (Figure 7d). This is clearly an effect of the keel, as calculations with uniform lithospheric thickness result in shorter-wavelength flow (Figure 4g for
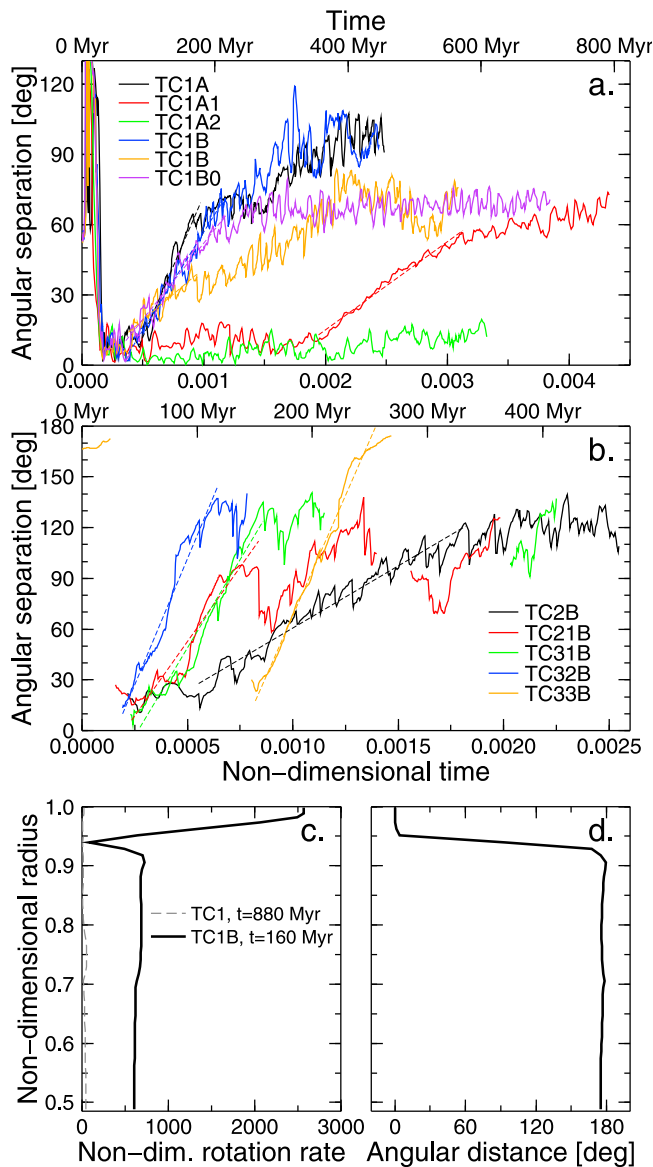
Figure 8. (a–b) Angular separation between the center of the lithospheric keel and the center of the thermal upwelling. Dashed lines fit the slope of the separation curves that were used to obtain the separation rates. Center of the plume is determined (a) at radius 2500 km, which is 120 km above the depth of viscosity layering for the 'TC1' cases, or (b) at the radius of viscosity layering (i.e., 2630 km for cases TC2B and TC21B, and 2880 km for cases TC31B, TC32B,and TC33B). In Figure 8b the separation is shown only for time intervals where degree 1 dominates the convective planform. (c) Rotation rate and (d) angular distance of rotation pole from the reference rotation pole of the surface, as a function of radius for cases TC1 at 880 Myr (time step 60,000; green curve) and TC1B at 160 Myr (15,000; blue curve).

case TC31). Rotation of the upwelling structure at a fast average rate of ~1.1°/Myr follows (Figure 8b). As soon as the lithosphere rotates ~90° away from the upwelling center, the upwelling structure stretches and breaks up into separate

plumes and eventually two strong upwellings develop in the hemisphere with thin lithosphere (Figure 10i).

[40] Case TC32B, which was started from time step 20,000 of case TC32, also develops a strong degree 1 (Figure 7e), unlike in the case with uniform lithosphere (Figure 4h for TC32), at $t \sim 40$ Myr, in the form of a plume cluster below the thick lithosphere. The lithosphere then rotates with respect to the plume cluster at average rate of ~1.5°/Myr (Figure 8b). Similar stretching and cluster breakup occurs as in TC31B.

[41] The initial state of case TC33B is an upwelling structure with dominant degree 1 (step 10,0000 of TC33). We placed the keel in a position antipodal to the upwelling center (Figure 10j). The flow field initially breaks up into a shorter-wavelength pattern, but at $t \sim 150$ Myr a broad cluster of plumes forms below the keel and degree 1 dominates the flow (Figures 7f and 10k). The presence of the keel therefore controls the flow geometry to the extent that it can flip a preexisting degree 1 structure by 180°. After the upwelling forms below the keel, a fast rotation of the lithosphere at a rate of ~1.5°/Myr follows (Figure 8b). In this case the plume structure does not stabilize near the keel boundary but the rotation continues until the stretched upwelling is approximately antipodal to the keel (Figure 10l). At that point the plume breaks into two separate upwellings.

[42] To summarize this section, we have found that the rotation of the lithosphere is a robust feature, present in all our models except those with a very small variations in lithospheric thickness. In order to excite the rotation of the lithospheric shell, the thickness variations have to be of the order of at least 100 km. A hemispheric variation in lithospheric thickness as little as tens of km is sufficient to focus the degree-1 thermal upwelling below the center of the hemisphere with thicker lithosphere. The presence of the lithospheric keel can also increase the wavelength of convection toward spherical harmonic degree 1, or reorient a preexisting degree-1 structure. We will further discuss the mechanism of the rotation and the rotation rates in section 5.2. In addition to cases with imposed lithospheric keel in one hemisphere, we have also investigated cases with hemispheric variation in near-surface thermal conductivity (i.e., imposing an insulating cap). These will also be presented in section 5.2.

5. Discussion

[43] The models presented in this study contain several aspects relevant to convection and mantle dynamics in general. We will address these first, before discussing more specific questions related to evolution of Mars.

5.1. What Determines Convective Wavelength?

[44] The fundamental question of what controls the preferred convective wavelength has been addressed by many authors, particularly in the view of large aspect ratio convection cells associated with plate tectonics on the Earth. Early studies investigated the effect of boundary conditions [*Chapman et al.*, 1980; *Hewitt et al.*, 1980] as well as the depth-dependent viscosity structure [*Jaupart and Parsons*, 1985]. First 3-D spherical shell convection models suggested a shift of spherical harmonic spectrum power to lower degrees by endothermic phase transition [*Tackley et al.*,
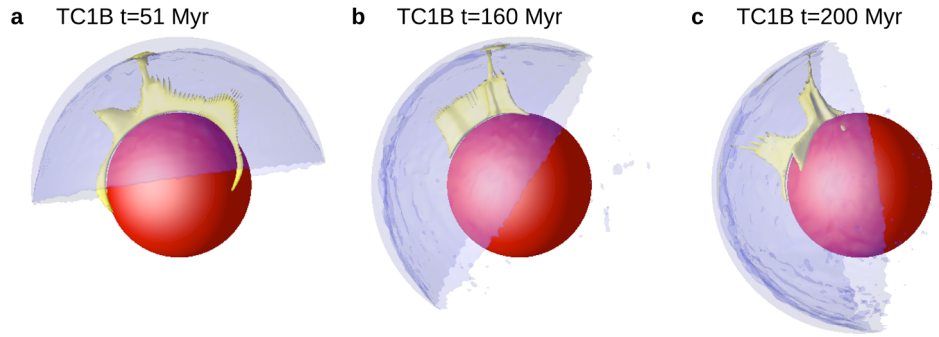
Figure 9. Isosurface of residual temperature at $T = +0.07$ in yellow and contour of the lithospheric keel, corresponding to residual composition isosurface at $C = -0.07$, in opaque blue. Temperature in the uppermost 120 km is not plotted. (a) TC1B at 51 Myr (time step 5000), (b) TC1B at 160 Myr (time step 15,000), (c) TC1B at 200 Myr (time step 20,000).

1993] or by viscosity increase from upper to lower mantle [*Bunge et al.*, 1996], even though the preferred wavelength they obtained was mostly at degree 6 or shorter, and is significantly smaller than the degree-2 planform indicated by global seismic tomography [e.g., *Ritsema et al.*, 1999], or even degree-1 flow suggested to have occurred over periods in Earth's history [*Zhong et al.*, 2007]. Upper to lower mantle viscosity increase combined with moderately strong plates is most likely responsible for the longest wavelength convection in the Earth's mobile lid regime [*Zhong et al.*, 2007]. For stagnant lid convection relevant for Mars, both viscosity layering [*Zhong and Zuber*, 2001] and endothermic phase change [*Harder and Christensen*, 1996] can produce degree-1 flow, even though very long time (several billion years) is required for the effect of phase transition to manifest [*Roberts and Zhong*, 2006].

[45] Our results from the suite of cases with uniform lithospheric thickness in section 3 are in accordance with previous studies that employed viscosity layering [*Zhong and Zuber*, 2001; *Roberts and Zhong*, 2006], but our models significantly broaden the region of parameter space by considering variation in depth of viscosity layering. With a step viscosity increase by a factor of 25 at depth 1020 km, degree 1 flow develops after a transient period of several hundred Myr. With decreasing thickness of the weak upper layer, a progressively weaker upper layer is necessary to produce degree-1 flow. This trade off between viscosity contrast and layering depth agrees with the analytical result of Figure 2 of *Zhong and Zuber* [2001].

[46] Even though we know empirically how to generate degree-1 flow in convection calculations, it remains unclear what determines the preferred convective wavelength. Ideally, one would hope for a fundamental theory that would, from a set of convection parameters (viscosity profile, Rayleigh number, etc.), predict the convective planform. Rayleigh-Taylor instability analysis in spherical axisymmetric geometry of *Zhong and Zuber* [2001] gives a regime diagram of dominant spherical harmonic degree as a function of viscosity contrast and depth of layering. It agrees reasonably well with results of numerical calculations, including the new results from this study. However, the Rayleigh-Taylor instability analysis for a simple two-layer

unstable system they used is only valid for small perturbations of the density interface depth at the onset of large-scale flow, and not for a steady state, finite-amplitude convection at supercritical Ra.

[47] For mobile lid convection, an analytical scaling law was derived by *Lenardic et al.* [2006], who based their approach on the classical boundary layer analysis, generalized for a setup with surface and basal weak channels. By maximizing surface heat flux they find that in the presence of the weak channels, the wavelength tends to increase with respect to an isoviscous case. They give an expression for the convection wavelength λ that maximizes the Nusselt number (their equation (10b))

$$\frac{\lambda}{2D} = \left[\frac{(d/D)^3}{\mu_r}\right]^{1/4}, \tag{7}$$

where d/D is the twice the channel thickness over the domain thickness and μ_r is the weak channel viscosity over the reference viscosity. In our notation, μ_r corresponds to $\mathcal{R}_\eta^{-1}$ and d is proportional to d_l. In order to maintain the longest wavelength (i.e., degree 1 in our spherical calculations), equation (7) suggests that $\mathcal{R}_\eta d_l^3 = const.$ or, in other words the dependence

$$\mathcal{R}_\eta \propto d_l^{-3}, \tag{8}$$

should describe the boundary between the domain of dominant spherical harmonic degree $l = 1$ (black circles) and $l > 1$ (gray crosses) in the regime diagram in Figure 5, if we assume that the same scaling holds for our stagnant lid models. The scaling law (8) is also implied by the results of *Ribe and de Valpine* [1994], who investigated Rayleigh-Taylor instability of the Earth's D″ layer. We have determined points to approximate the boundary between the two domains (small diamonds in Figure 5). For depths of viscosity layering 520 km and 770 km, we use points positioned midway on logarithmic scale between cases which produce degree-1 flow and cases with shorter dominant flow wavelength. For depth of layering 1020 km we also use results from *Roberts and Zhong* [2006]; we consider their case V2 (viscosity contrast $\mathcal{R}_\eta = 8$) as intermediate between
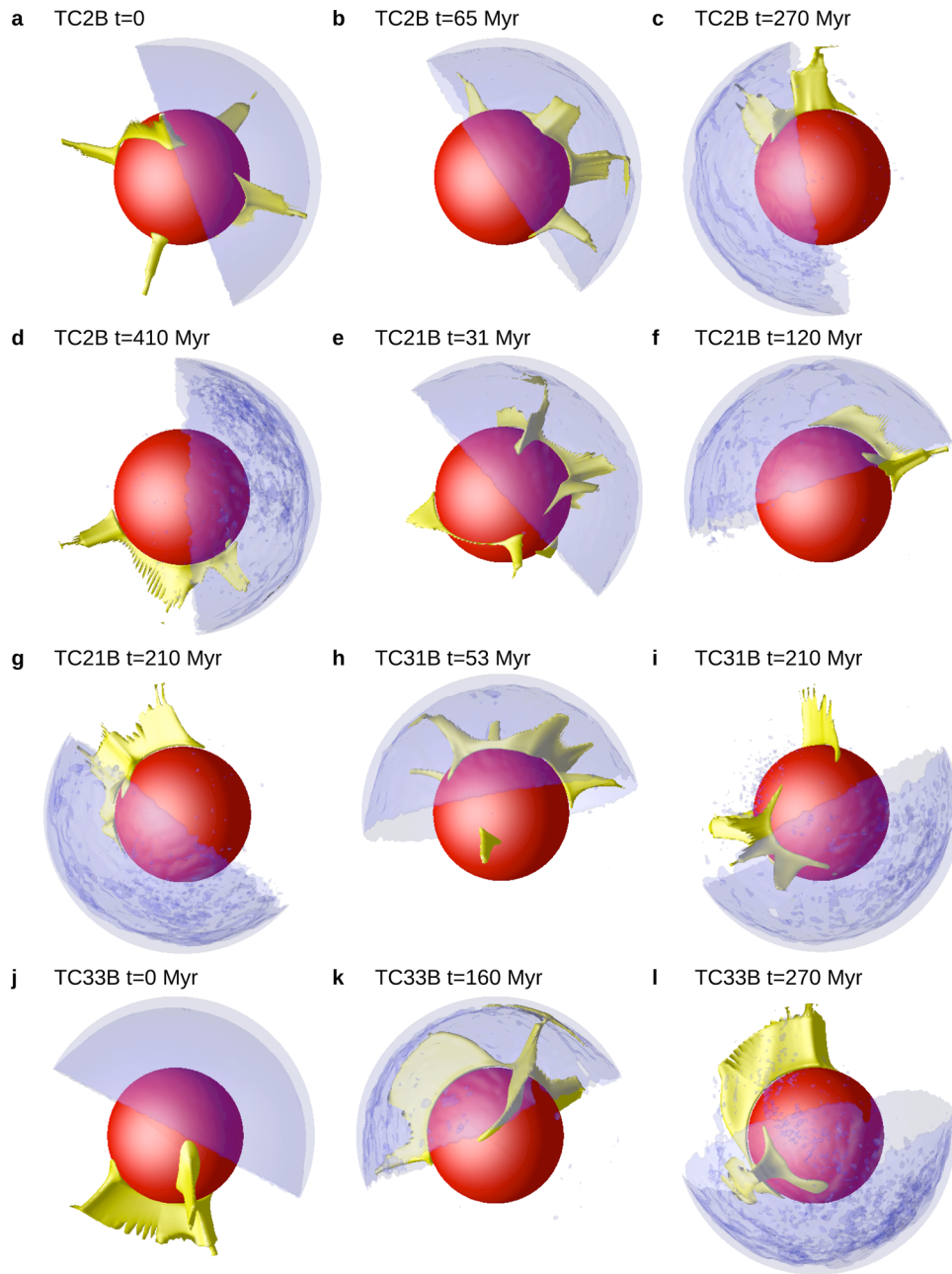
Figure 10. Isosurface of residual temperature at $T = +0.07$ in yellow and contour of the lithospheric keel, corresponding to residual composition isosurface at $C = -0.07$, in opaque blue. Temperature in the uppermost 120 km is not plotted. (a) TC2B initial state, (b) TC2B at 65 Myr (time step 5000), (c) TC2B at 270 Myr (25,000), (d) TC2B at 410 Myr (40,000), (e) TC21B at 35 Myr (3300), (f) TC21B at 120 Myr (15,000), (g) TC21B at 210 Myr (30,000), (h) TC31B at 53 Myr (5000), (i) TC31B at 210 Myr (20,000), (j) TC33B initial state, (k) TC33B at 160 Myr (20,000), and (l) TC33B at 270 Myr (41,000).

$l = 1$ and $l > 1$ and use it as the boundary point. The best least squares fit to the relation

$$\ln \mathcal{R}_\eta = a_0 + a_1 \ln d_l \qquad (9)$$

is found to give $\mathcal{R}_\eta = 0.0563 d_l^{-4.21}$ (plotted as dashed curve in Figure 5). We therefore obtain an exponent of larger magnitude than predicted by *Lenardic et al.* [2006], that is, a stronger dependence of $\mathcal{R}_a$ on d_l. We have used the depth of layering d_l from our model as the equivalent of the weak layer thickness d in the work of *Lenardic et al.* [2006]. However, our d_l also includes the thickness of the stagnant lithosphere, while *Lenardic et al.* [2006]'s setup does not include any high-viscosity surface layer. The thickness of the lithosphere L in our models is about 70 km. A least squares fit to equation (9) when we use a modified weak layer thickness $\tilde{d}_l = d_l - L$ yields an exponent -3.79, which is somewhat closer to, but still larger than the value 3 predicted by *Lenardic et al.* [2006].

[48] Additionally, relation (7) also predicts that for a given weak layer thickness, the preferred flow wavelength should vary as 4th root of the viscosity contrast, $\lambda \propto \sqrt[4]{\mathcal{R}_\eta}$. For example, by increasing the viscosity ratio by a factor of 8 from case TC3 to case TC33, the preferred wavelength should increase by a factor of only 1.7, according to equation (7). It is difficult to precisely define the flow wavelength for our 3-D spherical shell cases. However, the transition from predominantly spherical harmonic degree-4 flow in case TC3 (6 evenly distributed upwellings) to degree-1 flow in case TC33 (single upwelling) reflects a change of wavelength by a factor of around 4. Likewise, for cases TC2 and TC21 with viscosity ratio $\mathcal{R}_\eta$ changing from 25 to 50 (i.e., a factor of two), the predicted wavelength increase from equation (7) is only a factor of ~1.2, while our modeling results show a factor of 2 increase in wavelength from degree 2 to degree 1 for these two cases. This shows a much stronger dependence of convective wavelength on viscosity contrast than is predicted by equation (7).

[49] Even though the quantitative results for how convective wavelengths depend on the weak channel thickness and the viscosity contrast from our models are not in accord with *Lenardic et al.* [2006] analysis, we do obtain the same trend: a thinner weak channel requires a stronger viscosity contrast for degree-1 flow to develop. It is also important to point out that our cases were not specifically designed to test *Lenardic et al.* [2006]'s theoretical predictions on flow wavelength. For example, our models are in a spherical geometry with temperature-, pressure-, and depth-dependent viscosity, while *Lenardic et al.* [2006]'s analysis was for 2-D Cartesian models with only depth-dependent viscosity. The most important difference, however, is that *Lenardic et al.*'s [2006] theory was derived for mobile lid convection regime, while our models are stagnant lid cases. This is most likely the principal source of the discrepancy.

5.2. Why Plumes Form Below the Lithospheric Keel

[50] The first stage in models with imposed lithospheric keel involves concentration and focusing of upwellings below the keel. We have seen that imposition of the thick keel may even flip a preexisting degree-1 pattern by 180° over relatively short time (case TC33B). This may be explained by the insulating effect of the thick lithospheric keel that does not participate in convective motions and only permits vertical transport of heat by conduction, which results in warming of the underlying mantle relative to the opposite hemisphere. It is somewhat similar to the insulating effect of supercontinents on Earth [*Gurnis*, 1988; *Coltice et al.*, 2007], even though the situation in mobile lid convection is more complicated; here we do not have to consider direct geometrical modification of the flow by subduction at supercontinental edge.

[51] The imposition of the lithospheric keel does not change the surface heat flux immediately; it takes some time for the temperature field to adjust to the new flow geometry. As an example, in case TC1B the originally uniform (at long wavelength) surface heat flux shows a clear hemispheric pattern at $t = 100$ Myr where the heat flux averaged over the hemisphere with the keel is 25 % smaller than the heat flux average over the opposite hemisphere.

[52] In the original proposal by *Zhong* [2009], assuming an endogenic origin for the Martian crustal dichotomy, the keel represents the melt residue from partial melting that is responsible for generation of the thick crust in the present southern hemisphere. On the other hand, if the dichotomy was formed by a giant impact, no deep melting in the mantle below the thickened crust would be expected (we will explain this assumption later). The thicker crust in one hemisphere, with a high concentration of radiogenic heat sources relative to the mantle, would act as an insulating lid, but no stiff residue or thickened lithosphere would be present at depth below the thickened crust. To approximate this scenario, we ran cases with a surficial hemispheric cap with reduced thermal conductivity. Case TC1K has a cap 50 km thick where the thermal conductivity is reduced by a factor of 5. The initial temperature field (Figure 11a) is the same as for case TC1A. Within 100 Myr, an upwelling forms below the center of the low-conductivity lid (Figure 11b). Degree 1 becomes the strongest starting at $t = 55$ Myr. Similar development is seen in case TC1K1, where the thermal conductivity reduction is only by a factor 1.5 (Figure 11d). Such reduction in thermal conductivity results in similar hemispheric heat flux disparity as is produced by a keel of 260 km maximum thickness (e.g., case TC1B). As no lateral variations in lithospheric thickness are present in these cases, no lithospheric rotation is excited and the upwellings remain centered below the insulating cap (Figures 11c, 11e, and 11f). The implications of these results for Martian evolution will be discussed in section 5.4.

5.3. Why/How the Lithosphere Moves Relative to the Mantle

[53] Mobility of lithospheric blocks is intrinsic for the plate tectonics mode of mantle convection. The only surface motion admissible for one-plate planets in stagnant lid convection regime, relevant to Mars is a rotational motion of the entire stiff lithospheric shell with respect to the underlying mantle. This motion, analogous to the net rotation of the Earth's lithosphere [*Ricard et al.*, 1991; *Zhong*, 2001], represents degree-1 toroidal motion. Toroidal motion can only be excited by the poloidal, buoyancy-driven flow through coupling in the presence of lateral variations in viscosity [*Hager and O'Connell*, 1981], which are provided by the deep lithospheric keel for one-plate planets such as Mars [*Zhong*, 2009].

[54] All calculations are performed in the no-net-rotation reference frame [*Zhong et al.*, 2008]. To illustrate the lithospheric rotation relative to the mantle, Figure 8c shows the rotation rate of individual horizontal layers as a function of radius for case TC1 with uniform lithospheric thickness after degree-1 flow developed, and for case TC1B at an instant during the plume-keel separation stage (also see a similar plot in the work of *Zhong* [2009]). The rotation rates are negligible for case TC1 relative to TC1B. Rotation rates for case TC1B tend toward two distinct values, one for the upper ~100 km and the other for the mantle below ~300 km depth, with a transitional zone in between. The plot of angular distance of rotation poles of layers at different radii from the reference pole at the surface (Figure 8d) clearly shows the opposite sense of rotation of the lithosphere and the deeper mantle.

[55] The difference in average rotation of the single-plate lithosphere and the corresponding rotation of the mantle in opposite sense is the cause for the increasing separation

between the keel center and the upwelling center. When the upwelling gets near the keel edge, the relative motion between the lithosphere and the upwelling ceases. In many cases we observe that the lithosphere and the upwelling continue to rotate together while their angular separation remains approximately constant. See for example the snapshots c and d in Figure 10 for case TC2B (which are both taken from the same viewpoint, as well as the previous snapshots a and b of the same case). As this common rotation of the keel-plume system has to be compensated by an opposite rotation of the remaining mantle, it indicates that the position of the upwelling itself is generally not stationary with respect to the average mantle.

[56] The relative motion between the lithosphere and the mantle causes stretching of the upwelling in the direction of the motion, i.e., perpendicular to the keel edge, and the upwelling structure assumes an elongated, ridge-like shape. As discussed above, the thermal upwellings have a tendency to form preferentially below the center of the lithospheric keel. As a consequence, the positive thermal anomalies develop and get stronger at the side of the upwelling ridge closer to the keel center, and get weaker on the opposite side (i.e., further from the keel center), which effectively results in a motion of the upwelling relative to the mantle. The resulting rotation of the thermal anomaly in earlier stages is therefore intermediate between the rotation of the lithosphere and the average rotation of the mantle. This mechanism can also explain the cessation of the plume-lithosphere relative motion in later stages, when the upwelling stays effectively locked in with the lithosphere, and the two together rotate relative to the average mantle.

[57] Our results suggest that the separation rate between the keel and the upwelling center, or the rotation rate of lithosphere relative to the upwelling (see Table 3) is sensitive to the maximum keel thickness but mostly independent of the exact shape of the keel. This is apparent from comparison of the time-dependent angular separation for different cases in Figure 8a, where the depth of viscosity layering as well as the viscosity contrast are identical for all models, but the shape of the keel was varied. For example, the long-term trends for cases TC1A (black curve) and TC1B (blue curve) which have the same maximum thickness (260 km) but different keel shape, are very similar. Case TC1C with maximum keel thickness 160 km (orange curve) shows a slower average separation rate. Case TC1A1 with maximum keel thickness 130 km shows yet slower rate as well as a delay of separation onset by ~300 Myr. Finally, in case TC1A2 (maximum keel thickness 65 km) the upwelling remains centered below the keel (or possibly the yet slower separation is delayed by at least 400–500 Myr).

[58] Cases in Figure 8b with the same shape of the keel but variation in viscosity layering suggest that the separation rate is relatively insensitive to the depth of layering, but increases with increasing viscosity contrast. For example, the pairs of cases TC1 and TC2, or TC21 and TC31 with the same viscosity contrast but different thickness of the weak upper layer show similar plume-keel separation rates. On the other hand, the separation rate increases by a factor of about 2 from case TC2 to case TC21, and also from cases TC31 to TC32, for which the viscosity ratio is doubled. This increased separation rate with reduced viscosity for the weak layer is probably due to the reduced shear between the lithosphere and the bulk of the mantle. This trend is, however, not observed for cases TC32 and TC33 which show separation at comparable rates despite having different viscosity ratio.

[59] Another important factor affecting the separation rate is the buoyancy force available in the convective system that is also affected by viscosity structure. As the weak layer viscosity is further reduced, although the shear resisting force to the lithospheric rotation is reduced, it may also reduce the buoyancy force driving the lithospheric rotation. The competing effects of reduced shear resisting force and the buoyancy on lithospheric rotation need more studies in the future.

5.4. Implications for Mars

[60] The mutual orientation of the Martian crustal dichotomy and the Tharsis volcanic province has not been satisfactorily explained so far. In fact, common criticism of models that explain the origin of Tharsis by a mantle upwelling is that they do not explain its location near the dichotomy boundary [e.g., *Solomon et al.*, 2005].

[61] *Zhong*'s [2009] hypothesis offers an explanation of Tharsis current location relative to the crustal dichotomy and results of this study support this idea. The evolution of models with lithospheric keel are interpreted as follows. After the formation of the dichotomy, the Tharsis forming thermal upwelling would either have been already or start to first form below the center of the lithospheric keel or, in today's terms, near the south pole. At that point, the large thickness of the keel would prevent any melting in the upwelling plume, therefore no surface volcanism would occur. Assuming that the keel thickness decreases away from its center, the upwelling hot material would reach shallower depths at some point during the keel-plume separation stage. This would cause the plume temperature to be greater than the solidus and partial melt would be generated and extracted to the surface in the initial episode of Tharsis volcanism. As the separation between the keel and the plume increased, the volcanic center would move closer to the dichotomy boundary. The final, longest stage would involve stabilization of the upwelling near the dichotomy boundary, as inferred for the last ~4 Gyr and observed today. Because of the complicated plume morphology including multiple small plumes in the upper mantle originated from the sheared, elongated lower mantle plume perpendicular to the dichotomy boundary, the surface volcanism may have a rather complicated morphology with multiple volcanoes of similar ages or not necessarily a well defined age progression.

[62] This interpretation of the model bears on several assumptions, the most important being the presence of the lithospheric keel after the dichotomy formation. In the present calculations we impose the keel a priori. It remains to be shown in future work, that such lithosphere of variable thickness can be produced in convection models in a self-consistent fashion as a result of partial melting. *Keller and Tackley* [2009] are the first to have investigated the generation of Martian crust and its thickness variation in a global convection model. However, they did not consider devolatilization effects of partial melting and the modulation of the flow by the stiff melt residue.
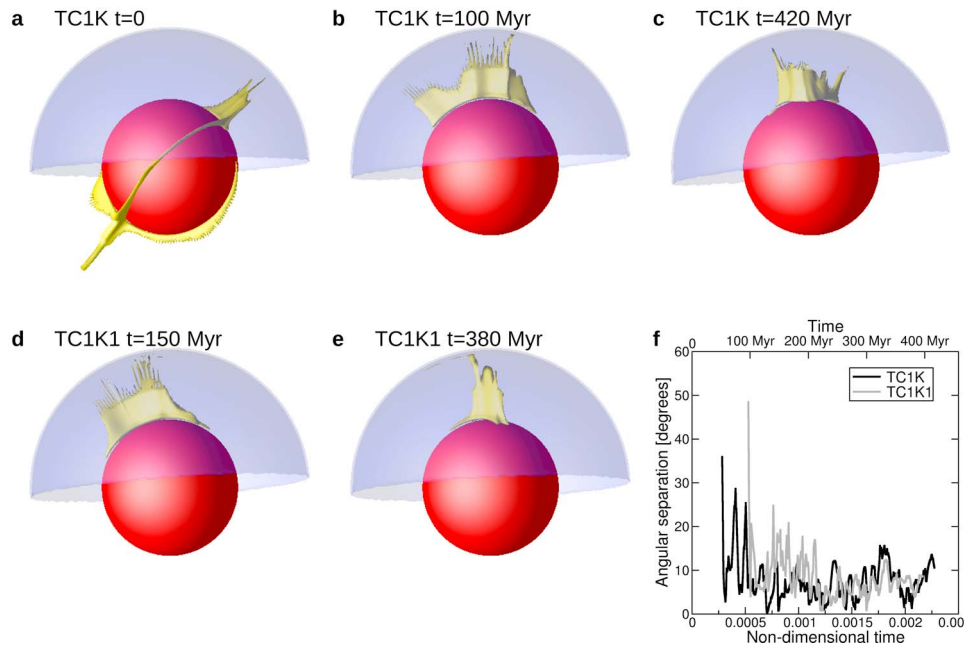
Figure 11. Isosurface of residual temperature at $T = +0.07$ in yellow and contour of the low-conductivity lid in opaque blue (Figures 11a–11e). Temperature in the uppermost 120 km is not plotted. (a) TC1K initial state, (b) TC1K at 100 Myr (time step 10,000), (c) TC1K at 420 Myr (time step 50,000), (d) TC1K1 at 150 Myr (time step 15,000), and (e) TC1K1 at 380 Myr (time step 45,000). (f) Center of the lid-plume separation.

[63] The keel formation in the proposed model is closely tied to the crustal dichotomy formation. The mean difference in crustal thickness between the two hemispheres of ~26 km [*Neumann et al.*, 2004] translates into a difference in basalt volume of $\sim 2 \times 10^9$ km³. A 10 % average melting of the mantle [*Hauck and Phillips*, 2002] responsible for the dichotomy formation would leave behind a melting residue layer of average thickness ~200 km; this value decreases with increasing average degree of melting. In order to form the dichotomy within 400 Myr of Mars formation [*Nimmo and Tanaka*, 2005], an average differential melt production of ~5 km³ yr⁻¹ between the two hemispheres is required. This is well within the values for possible total eruption rates of several tens of km³ yr⁻¹ in current dynamic melting models for Mars [*Breuer and Spohn*, 2006; *Keller and Tackley*, 2009].

[64] If the migration of Tharsis was indeed caused by the 'rotation of the lithosphere', we can constrain the thickness of the lithospheric keel. In order to explain the formation and migration of Tharsis within few hundred Myr after dichotomy formation, the lateral lithospheric thickness variation of at least ~200 km must be in place. There is no tight constraint on the keel shape from the time scales, but as was discussed above, a keel with decreasing thickness from the center outward would best explain, within this model, the absence of Tharsis-related volcanic structures in the southernmost latitudes of Mars.

[65] The requirement for the amplitude of the lithospheric thickness variation may also help distinguish between exogenic or endogenic origin of the dichotomy. Significant melting in the mantle at depths of few hundred km is intrinsic in the suggested endogenic mechanisms: both the degree-1 convection and the magma ocean cumulates overturn hypothesis and would generate thicker lithosphere in hemisphere with thicker crust (i.e., below southern highlands). Giant impact models predict redistribution of the crustal material so that thick crust is found in the hemisphere antipodal to the impact site. No melting of the deeper mantle accompanies this crustal thickening in that hemisphere. The thicker crust with a high concentration of heat-producing elements would effectively act as an insulating cap. As our models with a cap of reduced thermal conductivity (cases TC10K and TC10K1) show, thermal upwellings form below the cap center but the rotation of the lithosphere and, consequently, the migration of Tharsis are absent as there are no strong variations in lithospheric thickness. If mantle melting follows the impact, it takes place in the region below the impact [*Marinova et al.*, 2008; *Nimmo et al.*, 2008], which would result in lithosphere thickening below the impact basin (i.e., below northern lowlands). Consequently, the thermal upwelling would either form, remain stationary and cause volcanism below the center of thick crust (i.e., near the south pole), or alternately form below the thickened lithosphere in the north and migrate southward. Both alternatives are inconsistent with the observations. The 'rotation of the lithosphere model' would therefore strongly argue for an endogenic origin of the Martian dichotomy.

[66] Even though our models are primarily targeted at addressing questions of Martian dynamics, the results are generally applicable. In particular, they point at the importance of interaction between long-wavelength mantle convection in planetary interiors and lateral thickness variations of the lithosphere that can arise as a consequence of partial melting. In planetary mantles with a moderate viscosity

increase in the upper to midmantle depths, long-wavelength convection, including degree-1 convection, can develop in a relatively short time of few hundred Myr. The interaction between long-wavelength mantle convection and lithospheric thickness variations may excite lithospheric rotation with respect to the mantle, and cause plume-related volcanism to migrate on the planetary surfaces. In this study we have considered a predominantly degree-1 lithospheric thickness variation, with axially symmetrical keels of angular radius 90 degrees. This mantle flow lithosphere interaction mechanism may, however, operate at shorter dominant wavelengths too. To test this idea, we ran one model with two antipodal keels of angular radius 60° and maximum thickness 260 km but otherwise identical to case TC1A. This keel geometry imposes a corresponding increase in the dominant spherical harmonic of the flow from 1 (of the single-keel case TC1A) to 2, with one upwelling below each keel. The rotation of the lithosphere is also excited in the two-keel case. In general, the behavior may depend on the difference between the respective dominant wavelengths of the lithospheric thickness variations and of the convective structure. Apart from Mars, the lithospheric rotation may be potentially important for evolution of other terrestrial planetary bodies such as the Moon or the satellites of gas giants.

6. Conclusions

[67] In the present study, we used numerical modeling of convection in 3-D spherical shell to investigate in detail aspects of the 'rotation of the lithosphere' model for Mars [*Zhong*, 2009]. Our main findings can be summarized as follows.

[68] We investigated the conditions under which a spherical harmonic degree 1 flow is produced in the mantle of Mars in layered viscosity models with weak upper mantle. Moderate viscosity increase by a factor of 25 in the midmantle leads to degree-1 convection. With decreasing thickness of the weak layer, a progressively larger viscosity contrast is necessary for degree-1 flow. The trade off between the depth of layering d_l and the lower to upper layer viscosity ratio $\mathcal{R}_\eta$ necessary to produce degree-1 convection can be described by a power law $\mathcal{R}_\eta \propto d_l^{-\alpha}$ with the exponent α around 4.

[69] Introducing a hemispheric variation in lithospheric thickness, a lithospheric keel of hemispheric extent that represents melt residue after dichotomy formation process, results in formation and preferential orientation of upwellings in the hemisphere with thicker lithosphere. In cases where shorter wavelength flow (degree 2 or 3) arises with uniform lithospheric thickness, the presence of the lithospheric keel can organize the flow into a degree-1 pattern.

[70] If the maximum keel thickness is at least ~100 km in cases with 25-fold viscosity increase at 1000 km depth, a rotation of the entire lithospheric shell relative to the underlying mantle is excited, during which the angular distance between the lithospheric keel center and the position of upwelling increases from near 0 to near 90°. Similar behavior is observed for cases with a thinner weak layer. The separation rate seems to be controlled mostly by the amplitude of the lithospheric thickness variation and the magnitude of viscosity decrease in the weak layer, and is

relatively independent of the exact keel shape and the thickness of the weak channel. A keel of 260 km maximum thickness results in plume-keel separation rate of 0.7–1.5 degrees per Myr, depending on the viscosity structure.

[71] The relative motion between the lithosphere and the upwelling may explain the observed early migration of Tharsis volcanic center over the first few hundred Myr after its formation. Maximum keel thickness of at least ~200 km is required to explain the inferred Tharsis migration time scales.

[72] If the early migration of Tharsis was caused by this mechanism, the requirement on lithosphere thickness variation puts constrains on the dichotomy formation process. A few hundred km thick melt residue below the southern highlands can be produced by partial melting of upwelling mantle material, inherent in models of endogenic origin. An impact in the northern hemisphere is unlikely to produce the necessary lithospheric thickness variations in the southern hemisphere below the thickened crust.

References

Anderson, R. C., J. M. Dohm, M. P. Golombek, A. F. C. Haldemann, B. J. Franklin, K. L. Tanaka, J. Lias, and B. Peer (2001), Primary centers and secondary concentrations of tectonic activity through time in the western hemisphere of Mars, *J. Geophys. Res.*, *106*(E9), 20,563–20,585, doi:10.1029/2000JE001278.

Andrews-Hanna, J. C., M. T. Zuber, and W. B. Banerdt (2008), The Borealis basin and the origin of the martian crustal dichotomy, *Nature*, *453*(7199), 1212–1215, doi:10.1038/nature07011.

Banerdt, W. B., M. P. Golombek, and K. L. Tanaka (1992), Stress and tectonics on Mars, in *Mars*, edited by H. H. Kieffer et al., chap. 8, pp. 249–297, Univ. of Ariz. Press, Tucson.

Breuer, D., and T. Spohn (2006), Viscosity of the Martian mantle and its initial temperature: Constraints from crust formation history and the evolution of the magnetic field, *Planet. Space Sci.*, *54*(2), 153–169, doi:10.1016/j.pss.2005.08.008.

Breuer, D., H. Zhou, D. A. Yuen, and T. Spohn (1996), Phase transitions in the Martian mantle: Implications for the planet's volcanic history, *J. Geophys. Res.*, *101*(E3), 7531–7542, doi:10.1029/96JE00117.

Bunge, H.-P., M. A. Richards, and J. R. Baumgardner (1996), Effect of depth-dependent viscosity on the planform of mantle convection, *Nature*, *379*(6564), 436–438, doi:10.1038/379436a0.

Chapman, C. J., S. Childress, and M. R. E. Proctor (1980), Long wavelength thermal convection between non-conducting boundaries, *Earth Planet. Sci. Lett.*, *51*(2), 362–369, doi:10.1016/0012-821X(80)90217-4.

Christensen, U., and D. Yuen (1985), Layered convection induced by phase transitions, *J. Geophys. Res.*, *90*(B12), 10,291–10,300, doi:10.1029/JB090iB12p10291.

Coltice, N., B. R. Phillips, H. Bertrand, Y. Ricard, and P. Rey (2007), Global warming of the mantle at the origin of flood basalts over supercontinents, *Geology*, *35*(5), 391–394, doi:10.1130/G23240A.1.

Elkins-Tanton, L. T., E. M. Parmentier, and P. C. Hess (2003), Magma ocean fractional crystallization and cumulate overturn in terrestrial planets: Implications for Mars, *Meteoritics Planet. Sci.*, *38*(12), 1753–1771, doi:10.1111/j.1945-5100.2003.tb00013.x.

Elkins-Tanton, L. T., P. C. Hess, and E. M. Parmentier (2005), Possible formation of ancient crust in Mars through magma ocean processes, *J. Geophys. Res.*, *110*, E12S01, doi:10.1029/2005JE002480.

Frey, H. (1979), Thaumasia: A fossilized early forming Tharsis uplift, *J. Geophys. Res.*, *84*(B3), 1009–1023, doi:10.1029/JB084iB03p01009.

Frey, H. V. (2006a), Impact constraints on the age and origin of the lowlands of Mars, *Geophys. Res. Lett.*, *33*, L08S02, doi:10.1029/2005GL024484.

Frey, H. V. (2006b), Impact constraints on, and a chronology for, major events in early Mars history, *J. Geophys. Res.*, *111*, E08S91, doi:10.1029/2005JE002449.

Frey, H., and R. A. Schultz (1988), Large impact basins and the mega-impact origin for the crustal dichotomy on Mars, *Geophys. Res. Lett.*, *15*(3), 229–232, doi:10.1029/GL015i003p00229.

Frey, H., S. E. Sakimoto, and J. Roark (1998), The MOLA topographic signature at the crustal dichotomy boundary zone on Mars, *Geophys. Res. Lett.*, *25*(24), 4409–4412, doi:10.1029/1998GL900095.

Gurnis, M. (1988), Large-scale mantle convection and the aggregation and dispersal of supercontinents, *Nature*, *332*(6166), 695–699, doi:10.1038/332695a0.

Hager, B. H., and R. J. O'Connell (1981), A simple global model of plate dynamics and mantle convection, *J. Geophys. Res.*, *86*(B6), 4843–4867, doi:10.1029/JB086iB06p04843.

Harder, H., and U. R. Christensen (1996), A one-plume model of martian mantle convection, *Nature*, *380*(6574), 507–509, doi:10.1038/380507a0.

Hartmann, W. K. (1973), Martian surface and crust: Review and synthesis, *Icarus*, *19*(4), 550–575, doi:10.1016/0019-1035(73)90083-3.

Hauck, S. A., II, and R. J. Phillips (2002), Thermal and crustal evolution of Mars, *J. Geophys. Res.*, *107*(E7), 5052, doi:10.1029/2001JE001801.

Head, J. W., III, M. A. Kreslavsky, and S. Pratt (2002), Northern lowlands of Mars: Evidence for widespread volcanic flooding and tectonic deformation in the Hesperian Period, *J. Geophys. Res.*, *107*(E1), 5003, doi:10.1029/2000JE001445.

Hewitt, J. M., D. P. McKenzie, and N. O. Weiss (1980), Large aspect ratio cells in two-dimensional thermal convection, *Earth Planet. Sci. Lett.*, *51*(2), 370–380, doi:10.1016/0012-821X(80)90218-6.

Hirth, G., and D. L. Kohlstedt (1996), Water in the oceanic upper mantle: implications for rheology, melt extraction and the evolution of the lithosphere, *Earth Planet. Sci. Lett.*, *144*(1–2), 93–108, doi:10.1016/0012-821X(96)00154-9.

Jaupart, C., and B. Parsons (1985), Convective instabilities in a variable viscosity fluid cooled from above, *Phys. Earth Planet. Int.*, *39*(1), 14–32, doi:10.1016/0031-9201(85)90112-8.

Johnson, C. L., and R. J. Phillips (2005), Evolution of the Tharsis region of Mars: Insights from magnetic field observations, *Earth Planet. Sci. Lett.*, *230*(3–4), 241–254, doi:10.1016/j.epsl.2004.10.038.

Ke, Y., and V. S. Solomatov (2006), Early transient superplumes and the origin of the Martian crustal dichotomy, *J. Geophys. Res.*, *111*, E10001, doi:10.1029/2005JE002631.

Keller, T., and P. J. Tackley (2009), Towards self-consistent modeling of the Martian dichotomy: The influence of one-ridge convection on crustal thickness distribution, *Icarus*, *202*(2), 429–443, doi:10.1016/j.icarus.2009.03.029.

King, S. D. (2010), More speculations on the origin of the Tharsis Rise, *Lunar Planet. Sci.*, *XVI*, Abstract 2007.

King, S. D., and D. L. Anderson (1998), Edge-driven convection, *Earth Planet. Sci. Lett.*, *160*(3-4), 289–296, doi:10.1016/S0012-821X(98)00089-2.

King, S. D., and H. L. Redmond (2005), The crustal dichotomy and edge driven convection: A mechanism for Tharsis Rise volcanism?, *Lunar Planet. Sci.*, *XXXVI*, Abstract 1960.

Lenardic, A., F. Nimmo, and L. Moresi (2004), Growth of the hemispheric dichotomy and the cessation of plate tectonics on Mars, *J. Geophys. Res.*, *109*, E02003, doi:10.1029/2003JE002172.

Lenardic, A., M. A. Richards, and F. H. Busse (2006), Depth-dependent rheology and the horizontal length scale of mantle convection, *J. Geophys. Res.*, *111*, B07404, doi:10.1029/2005JB003639.

Lingenfelter, R. E., and G. Schubert (1973), Evidence for convection in planetary interiors from first-order topography, *Earth, Moon, and Planets*, *7*(1), 172–180, doi:10.1007/BF00578814.

Marinova, M. M., O. Aharonson, and E. Asphaug (2008), Mega-impact formation of the Mars hemispheric dichotomy, *Nature*, *453*(7199), 1216–1219, doi:10.1038/nature07070.

McGill, G. E., and A. M. Dimitriou (1990), Origin of the Martian global dichotomy by crustal thinning in the late Noachian or early Hesperian, *J. Geophys. Res.*, *95*(B8), 12,595–12,605, doi:10.1029/JB095iB08p12595.

McNamara, A. K., and S. Zhong (2004), Thermochemical structures within a spherical mantle: Superplumes or piles?, *J. Geophys. Res.*, *109*, B07402, doi:10.1029/2003JB002847.

Mège, D., and P. Masson (1996), A plume tectonics model for the Tharsis province, Mars, *Planet. Space Sci.*, *44*(12), 1499–1546, doi:10.1016/S0032-0633(96)00113-4.

Mutch, T. A., and R. S. Saunders (1976), The geologic development of Mars: A review, *Space Sci. Rev.*, *19*(1), 3–57, doi:10.1007/BF00215628.

Neumann, G. A., M. T. Zuber, M. A. Wieczorek, P. J. McGovern, F. G. Lemoine, and D. E. Smith (2004), Crustal structure of Mars from gravity and topography, *J. Geophys. Res.*, *109*, E08002, doi:10.1029/2004JE002262.

Nimmo, F., and K. Tanaka (2005), Early crustal evolution of Mars, *Annu. Rev. Earth Planet. Sci.*, *33*(1), 133–161, doi:10.1146/annurev.earth.33.092203.122637.

Nimmo, F., S. D. Hart, D. G. Korycansky, and C. B. Agnor (2008), Implications of an impact origin for the martian hemispheric dichotomy, *Nature*, *453*(7199), 1220–1223, doi:10.1038/nature07025.

Phillips, R. J., et al. (2001), Ancient geodynamics and global-scale hydrology on Mars, *Science*, *291*(5513), 2587–2591, doi:10.1126/science.1058701.

Picardi, G., et al. (2005), Radar soundings of the subsurface of Mars, *Science*, *310*(5756), 1925–1928, doi:10.1126/science.1122165.

Pollack, H. N. (1986), Cratonization and thermal evolution of the mantle, *Earth Planet. Sci. Lett.*, *80*(1–2), 175–182, doi:10.1016/0012-821X(86)90031-2.

Purucker, M., D. Ravat, H. Frey, C. Voorhies, T. Sabaka, and M. Acuña (2000), An altitude-normalized magnetic map of Mars and its interpretation, *Geophys. Res. Lett.*, *27*(16), 2449–2452, doi:10.1029/2000GL000072.

Reese, C. C., C. P. Orth, and V. S. Solomatov (2010), Impact origin for the Martian crustal dichotomy: Half emptied or half filled?, *J. Geophys. Res.*, *115*, E05004, doi:10.1029/2009JE003506.

Ribe, N. M., and D. P. de Valpine (1994), The global hotspot distribution and instability of D″, *Geophys. Res. Lett.*, *21*(14), 1507–1510, doi:10.1029/94GL01168.

Ricard, Y., C. Doglioni, and R. Sabadini (1991), Differential rotation between lithosphere and mantle: A consequence of lateral mantle viscosity variations, *J. Geophys. Res.*, *96*(B5), 8407–8415, doi:10.1029/91JB00204.

Ritsema, J., H. J. v. Heijst, and J. H. Woodhouse (1999), Complex shear wave velocity structure imaged beneath Africa and Iceland, *Science*, *286*(5446), 1925–1928, doi:10.1126/science.286.5446.1925.

Roberts, J. H., and S. Zhong (2006), Degree-1 convection in the Martian mantle and the origin of the hemispheric dichotomy, *J. Geophys. Res.*, *111*, E06013, doi:10.1029/2005JE002668.

Schubert, G., and R. E. Lingenfelter (1973), Martian centre of mass - centre of figure offset, *Nature*, *242*(5395), 251–252, doi:10.1038/242251a0.

Sleep, N. H. (1994), Martian plate tectonics, *J. Geophys. Res.*, *99*(E3), 5639–5655, doi:10.1029/94JE00216.

Smith, D. E., et al. (1998), Topography of the northern hemisphere of Mars from the Mars Orbiter Laser Altimeter, *Science*, *279*(5357), 1686–1692, doi:10.1126/science.279.5357.1686.

Smith, D. E., et al. (1999a), The global topography of Mars and implications for surface evolution, *Science*, *284*(5419), 1495–1503, doi:10.1126/science.284.5419.1495.

Smith, D. E., W. L. Sjogren, G. L. Tyler, G. Balmino, F. G. Lemoine, and A. S. Konopliv (1999b), The gravity field of Mars: Results from Mars Global Surveyor, *Science*, *286*(5437), 94–97, doi:10.1126/science.286.5437.94.

Smith, D. E., et al. (2001), Mars Orbiter Laser Altimeter: Experiment summary after the first year of global mapping of Mars, *J. Geophys. Res.*, *106*(E10), 23,689–23,722, doi:10.1029/2000JE001364.

Solomon, S. C., et al. (2005), New perspectives on ancient Mars, *Science*, *307*(5713), 1214–1220, doi:10.1126/science.1101812.

Tackley, P. J., and S. D. King (2003), Testing the tracer ratio method for modeling active compositional fields in mantle convection simulations, *Geochem. Geophys. Geosyst.*, *4*(4), 8302, doi:10.1029/2001GC000214.

Tackley, P. J., D. J. Stevenson, G. A. Glatzmaier, and G. Schubert (1993), Effects of an endothermic phase transition at 670 km depth in a spherical model of convection in the Earth's mantle, *Nature*, *361*(6414), 699–704, doi:10.1038/361699a0.

Tanaka, K. (1986), The stratigraphy of Mars, *Proc. Lunar Planet. Sci. Conf. 17th*, Part 1, *J. Geophys. Res.*, *91*, suppl., E139–E158, doi:10.1029/JB091iB13p0E139.

Tanaka, K. L., D. H. Scott, and R. Greeley (1992), Global stratigraphy, in *Mars*, edited by H. H. Kieffer et al., chap. 11, pp. 345–382, Univ. of Ariz. Press, Tucson.

Tyler, G. L., G. Balmino, D. P. Hinson, W. L. Sjogren, D. E. Smith, R. Woo, S. W. Asmar, M. J. Connally, C. L. Hamilton, and R. A. Simpson (1992), Radio science investigations with Mars Observer, *J. Geophys. Res.*, *97*(E5), 7759–7779, doi:10.1029/92JE00513.

Watters, T. R., P. J. McGovern, and R. P. Irwin III (2007), Hemispheres apart: The crustal dichotomy on Mars, *Annu. Rev. Earth Planet. Sci.*, *35*(1), 621–262, doi:10.1146/annurev.earth.35.031306.140220.

Wilhelms, D. E., and S. W. Squyres (1984), The Martian hemispheric dichotomy may be due to a giant impact, *Nature*, *309*(5964), 138–140, doi:10.1038/309138a0.

Wise, D. U., M. P. Golombek, and G. E. McGill (1979), Tharsis province of Mars: Geologic sequence, geometry, and a deformation mechanism, *Icarus*, *38*(3), 456–472, doi:10.1016/0019-1035(79)90200-8.

Withers, P., and G. A. Neumann (2001), Enigmatic northern plains of Mars, *Nature*, *410*(6829), 651–651, doi:10.1038/35070640.

Zhong, S. (2001), Role of ocean-continent contrast and continental keels on plate motion, net rotation of lithosphere, and the geoid, *J. Geophys. Res.*, *106*(B1), 703–712, doi:10.1029/2000JB900364.

Zhong, S. (2009), Migration of Tharsis volcanism on Mars caused by differential rotation of the lithosphere, *Nat. Geosci.*, *2*(1), 19–23, doi:10.1038/ngeo392.

Zhong, S., and M. T. Zuber (2001), Degree-1 mantle convection and the crustal dichotomy on Mars, *Earth Planet. Sci. Lett.*, *189*(1–2), 75–84, doi:10.1016/S0012-821X(01)00345-4.

Zhong, S., M. T. Zuber, L. Moresi, and M. Gurnis (2000), Role of temperature-dependent viscosity and surface plates in spherical shell models of mantle convection, *J. Geophys. Res.*, *105*(B5), 11,063–11,082, doi:10.1029/2000JB900003.

Zhong, S., N. Zhang, Z.-X. Li, and J. H. Roberts (2007), Supercontinent cycles, true polar wander, and very long-wavelength mantle convection, *Earth Planet. Sci. Lett.*, *261*(3–4), 551–564, doi:10.1016/j.epsl.2007.07.049.

Zhong, S., A. McNamara, E. Tan, L. Moresi, and M. Gurnis (2008), A benchmark study on mantle convection in a 3-D spherical shell using CitcomS, *Geochem. Geophys. Geosyst.*, *9*, Q10017, doi:10.1029/2008GC002048.

Zuber, M. T., D. E. Smith, S. C. Solomon, D. O. Muhleman, J. W. Head, J. B. Garvin, J. B. Abshire, and J. L. Bufton (1992), The Mars Observer Laser Altimeter investigation, *J. Geophys. Res.*, *97*(E5), 7781–7797, doi:10.1029/92JE00341.

Zuber, M. T., et al. (2000), Internal structure and early thermal evolution of Mars from Mars Global Surveyor topography and gravity, *Science*, *287*(5459), 1788–1793, doi:10.1126/science.287.5459.1788.

O. Šrámek and S. Zhong, Department of Physics, University of Colorado at Boulder, 390 UCB, Boulder, CO 80309-0390, USA. (ondrej.sramek@colorado.edu)